2014-01-27

The Effect of Inlet Conditions on the Turbulent Wake of a Surface Mounted Fence

Wei, Xiaojian

UNIVERSITY OF CALGARY

The Effect of Inlet Conditions on the Turbulent Wake of a Surface Mounted Fence

by

Xiaojian Wei

A THESIS

SUBMITTED TO THE FACULTY OF GRADUATE STUDIES

IN PARTIAL FULFILLMENT OF THE REQUIREMENTS FOR THE

DEGREE OF MASTERS OF SCIENCE

DEPARTMENT OF MECHANICAL ENGINEERING

CALGARY, ALBERTA

January, 2014

Abstract

This thesis analyses the flow over a surface mounted fence (SMF) with two different inlet conditions. The fence causes a large modification of the inlet flow. Two different types of instabilities affect this flow geometry: the Kelvin-Helmholtz instability (K-H) in the separated shear layer and a 'shedding-type' instability which affects the entire recirculation region. In this study, two δ/h ratios are investigated while maintaining the same Reynolds number. It was hypothesized that the δ/h ratio affects the frequency of the K-H instability and subsequently the 'shedding-type' instability. Time-averaged flow fields were compared between the two cases. In an unsteady analysis, the Strouhal number of the dominant frequency of the K-H instability was investigated. The Strouhal number varied between the two due to velocity gradient at the separation point. The 'shedding-type' instability was also investigated and was found to be intermittent.

Acknowledgements

Table of Contents

List of Tables

List of Figures and Illustrations

List of Symbols, Abbreviations and Nomenclature

Abbreviation	Definition
SMF	surface-mounted fence
BFS	backward-facing step
FFS	forward-facing step
ER	expansion ratio
LES	large eddy simulation
K-H	Kelvin-Helmholtz
PIV	particle Image velocimetry
BL	boundary layer
FFT	Fast Fourier Transform
EMD	empirical mode decomposition
IMF	intrinsic mode function

Symbol	Definition
δ	boundary layer thickness
x_f	incoming boundary layer separation length
X_r	time-averaged reattachment length
Re_h	Reynolds number based on fence height
h	fence height
U_∞	freestream velocity
ν	kinematic viscosity
W_1	tunnel height upstream of the step
W_2	tunnel height downstream of the step
u'	streamwise velocity fluctuations

v'	vertical velocity fluctuations
Re_θ	Reynolds number based on momentum thickness
H	depth of the water channel
B	width of the water channel
Tu	turbulent intensity
α	fence sweep angle
X_s	length of the secondary recirculation
St_θ	Strouhal number based on momentum thickness
f_{K-H}	Kelvin-Helmholtz frequency
θ_c	momentum thickness at the separation point
U_c	convection velocity at the separation point
St_{shed}	universal Strouhal number
f_{shed}	shedding frequency of large scale vortex structures
Y_b	maximum height of the recirculation region
U_s	velocity at fence separation point
St_h	Strouhal number based on fence height
Stk	Stokes number
τ_p	relaxation time of the seeding particle
τ	characteristic time scale of the flow
u_s	settling time of the particle
g	gravitational acceleration
T	Water Temperature
x	Distance between rod position and fence position
δ^*	Displacement thickness
$H^\star$	Shape factor
$\chi\omega$	Reverse flow parameter at the wall

$\overline{u}$	time-averaged streamwise velocity
$\overline{\omega}_z$	spanwise vorticity
u_{rms}	root-mean-square velocity
h_1	intrinsic mode function
r_1	residue function

Chapter 1

Introduction

1.1 Objective

The province of Alberta in Canada is situated next to the large Rocky Mountain range. The westerly winds which buffet the Rocky Mountains are an excellent wind energy resource. Several wind farms are already located in southern Alberta adjacent to the mountains. However, flow over mountainous terrain is very turbulent, requiring an in-depth analysis of the flow downstream of the mountains. The mean flow features over mountainous terrain are shown in Figure 1.1.
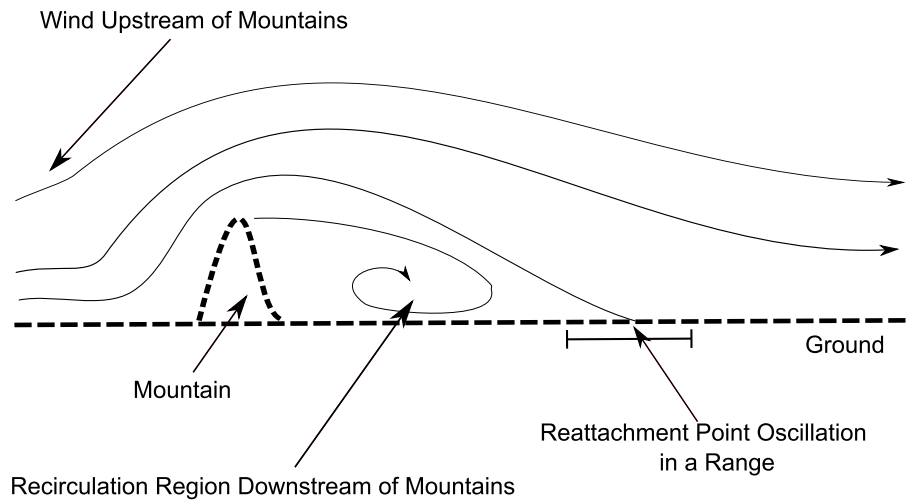
Figure 1.1: Side view of mountainous flow, where the flow separates from the mountain ridge, forming a separated shear layer and a recirculation region before reattaching on the ground. The reattachment point of the shear layer oscillates periodically in a oscillation zone due to unsteadiness of the flow.

The unsteadiness of the wind flow over the Rocky Mountains is important for wind power forecasting in the province of Alberta. A change in wind speed from one value to another

over a designated period is known as a wind ramp event, as shown by Sevlian and Rajagopal (2012). The intensity of the wind ramp event can then be characterised by the degree of change over a certain time period. Wind ramp events were measured at a wind mast operated by the University of Calgary downstream of the Rocky Mountains. Characterisation of such wind ramp events is thus important for future deployment of further wind farms in Alberta. The period of the ramp events varies throughout the day and can be partly attributed to the diurnal temperature variation. It is likely, the temperature variation will alter the buoyancy forces and hence the atmospheric boundary layer thickness upstream of the mountain ridges.

Flow over a mountainous ridge (see Figure 1.1) exhibits many flow features of a bluff body separating and reattaching flow field. The turbulent structures and wind speed fluctuations created by the ridge will affect the energy extraction of wind turbines sited downstream as in Southern Alberta. It is thus important to characterise the flow field downstream of mountainous ridges.

1.2   Experiment model

In this study, a surface-mounted fence (SMF) is used to model mountainous terrain. As a separating and reattaching flow, the average flow topology created by a SMF is shown in Figure 1.2. The inlet flow with boundary layer thickness, δ, separates at a distance of x_f upstream to the fence due to an adverse pressure gradient caused by the fence blockage. This separation creates an upstream recirculation region which rotates in a clockwise direction. An intense separated shear layer deflects into the freestream from the fence top. The separated shear layer reattaches on the bottom wall at a mean distance of X_r. However, the reattachment position oscillates in a reattachment zone due to the unsteady flapping motion of the shear layer. The separated shear layer bounds the primary recirculation region rotating in a clockwise direction. A secondary recirculation regions forms adjacent to the downstream wall of the fence due to the induced flow by the primary recirculation region.

The secondary recirculation region rotates in an anti-clockwise direction. The average flow features of the SMF flow field are thus an upstream recirculation region and a separated shear layer bounding a primary and secondary recirculation region.
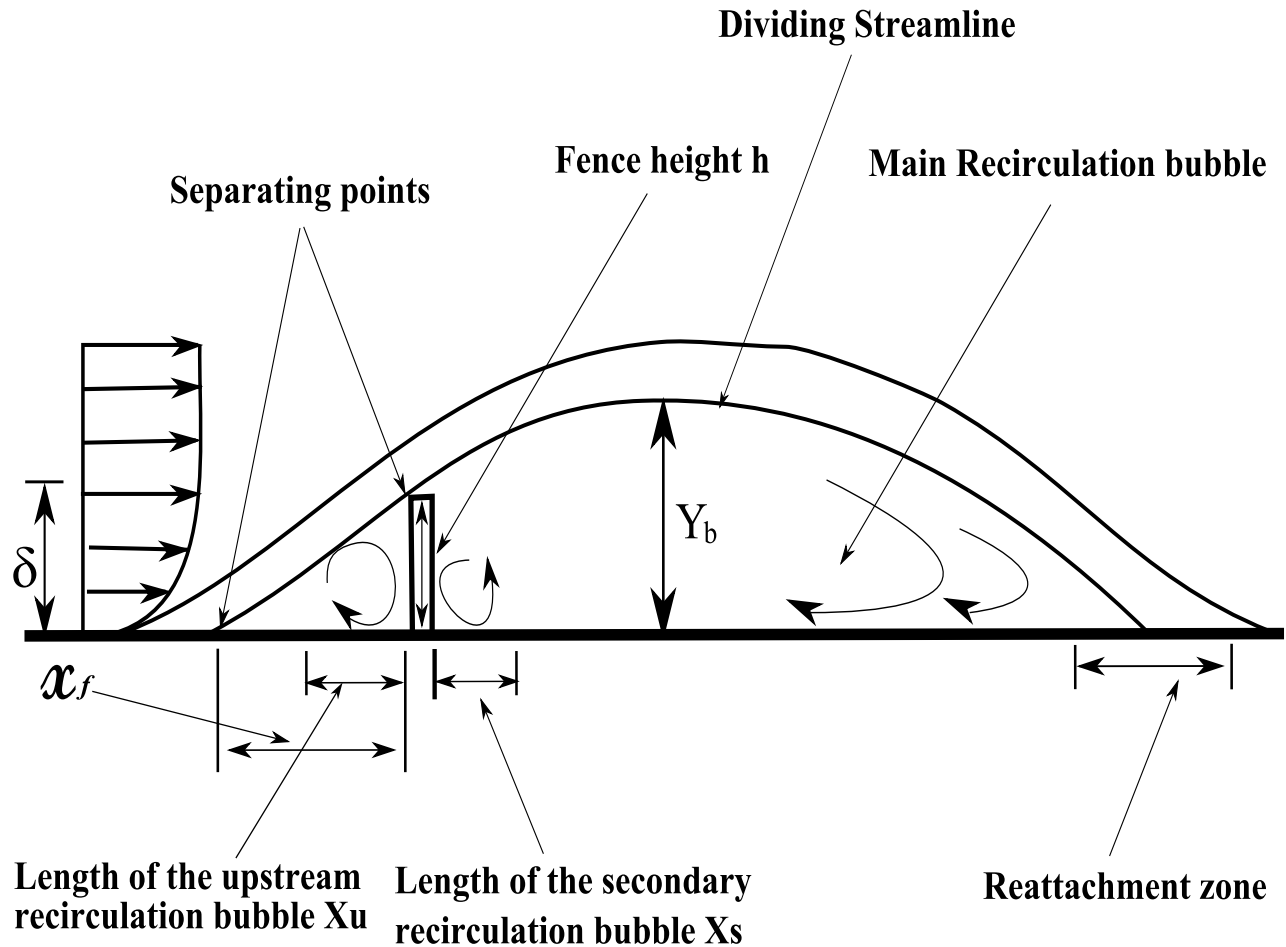
Figure 1.2: Average flow features of surface-mounted fence flow. The incoming boundary layer separates upstream of the fence forming an upstream recirculation region. An intense separated shear layer forms at the edge of the fence with a secondary recirculation region closer to the fence and a main recirculation region forming below the separated shear layer. The separated shear layer reattaches in the reattachment zone at an average length of $13.45h$ at $Re_h = 10\,500$; as discussed by Orellano and Wengle (2000).

1.3 Separating-reattaching flows

The flow features of the SMF flow are analagous in many ways to several other bluff body separating and reattaching flow fields. These include flows over sudden expansion or constriction geometries, such as backward-facing step (BFS) and forward-facing step (FFS) flows. The flow features of each geometry will be critically analysed in the following section.

1.3.1 Flow over a backward-facing step

One of the simplest separating and reattaching flows is that over a BFS. A schematic of the mean flow features over a BFS is shown in Figure 1.3.
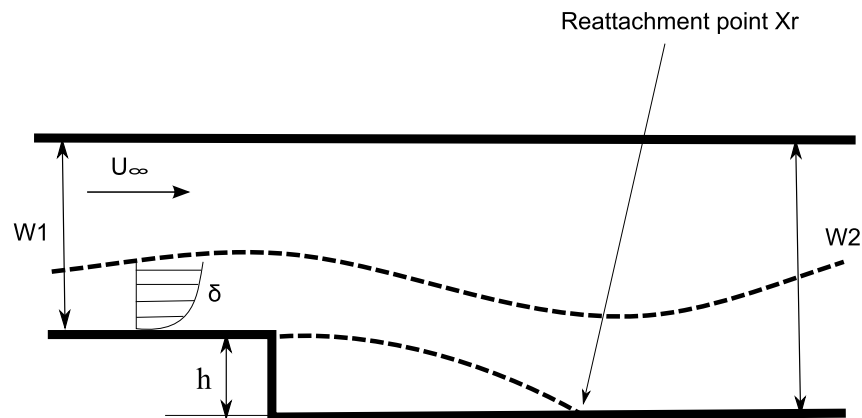
Figure 1.3: The geometry of a backward facing step with important flow parameters (Adams and Johnston, 1988).

The inlet boundary layer of thickness δ approaches the expansion from the left. The flow separates from the step edge and a shear layer forms. The separated shear layer is initially parallel with the freestream flow, it then curves downwards until it reattaches on the bottom wall at a mean length of X_r. The shear layer encompasses a recirculation region which interacts with the shear layer. Adams and Johnston (1988) summarized the dimensionless parameters which affect the BFS flow as the Reynolds number (Re_h), the expansion ratio (ER) and the boundary layer thickness to step height ratio (δ/h). The Reynolds number,

Re_h, as defined in Equation 1.1 represents the ratio of inertial to viscous forces:

$$Re_h = \frac{U_\infty \times h}{\nu},\qquad(1.1)$$

where U_∞ is the inlet freestream velocity, h is the step height and ν is the kinematic viscosity. Armaly et al. (1983) found that the reattachment length (X_r/h) increases with Re_h up to approximately $Re_h = 1\,200$, decreased in the transitional range $1\,200 < Re_h < 6\,600$, and remained relatively constant when the flow became fully turbulent at $Re_h > 6\,600$.

The expansion ratio, ER, which acts as the geometry parameter; is defined in Equation 1.2 by Adams and Johnston (1988),

$$ER = W_2/W_1,\qquad(1.2)$$

where W_1 and W_2 are the channel heights upstream and downstream of the step as shown in Figure 1.3. In the turbulent range $(Re_h > 6\,600)$, De Brederode and Bradshaw (1972) found that $X_r = 6h$ at an ER of 1.2, whereas Moss et al. (1979) found that $X_r = 5.5h$ at an ER of 1.1. This shows that at this Re_h the reattachment length decreases with a decreasing expansion ratio (Armaly et al., 1983).

The ratio of inlet boundary layer thickness, δ, to step height, h characterises the impact of the upstream conditions. Adams and Johnston (1988) investigated the Re_h range of $8\,000 < Re_h < 40\,000$ and a range of boundary layer thickness of $0.005 < \delta/h < 1.7$ at an expansion ratio of 2.5. δ is calculated as the vertical position where $u(y) = 0.99U_\infty$. At $Re_h = 36\,000$, the δ/h ratio changed from 0.005 to 1.7 and the upstream boundary layer underwent a transition from laminar to turbulent accordingly. It was found that the reattachment length (X_r/h) increased by 30% when the upstream boundary layer changes from laminar to turbulent flow. This trend was also found at other Re_h from $8\,000$ to $26\,000$. It was discussed by Adams and Johnston (1988) that the changes of the reattachment length between laminar and turbulent upstream boundary layer come from the different growth rate

of the free-shear layer just after separation. It was found by Bradshaw (1966) that at high Re_h the value of $\overline{u'v'}$ in the initial stage of the free shear layer with laminar initial conditions is higher than with turbulent initial conditions. Therefore, in the BFS research by Adams and Johnston (1988), the free-shear layers at the step with a laminar boundary layer had a higher entrainment than the free shear layer with a turbulent boundary layer. The higher entrainment in the free-shear layer will cause a shorter reattachment length; as discussed by Chapman et al. (1958).

Eaton and Johnston (1981) and Durst and Tropea (1981) separately studied the Reynolds number based of momentum thickness, Re_θ, and step height, Re_h. Although Re_h includes no information about the upstream flow, it represents the ratio of inertial to viscous forces, where h is used as the most obvious physical length scale when non-dimensionalizing the Navier-Stokes equations (Adams and Johnston, 1988). The reason why Re_θ has not been applied as a parameter representing the upstream boundary layer is that δ/h can highly correlate upstream initial conditions; as shown by Adams and Johnston (1988). Using these past studies as a guide, we set Re_h to be constant and change the δ/h ratio to investigate the effect of inlet conditions on the flow downstream of a SMF.

The unsteady motions in the BFS flow field, have also received attention. Friedrich and Arnal (1990) using a large eddy simulation (LES), determined that the separated shear layer moved in a vertical motion, causing the reattachment location to oscillate. Le et al. (1997) further showed that in BFS flow the shear layer rolled up forming a large-scale vortex behind the step. When this large-scale vortex structure grew, the reattachment point moved downstream at a nearly constant speed, then after the large scale structure detached, the reattachment point moved back upstream quickly.

1.3.2 Flow over a forward-facing step

A more complex separating and reattaching flow than the BFS is that over a FFS. As shown in Figure 1.4, in a FFS flow, the turbulent boundary layer separates upstream of the step

face due to an adverse pressure gradient caused by the blockage of the step. Leclercq et al. (2001) found the flow separates 1-1.2h upstream of the step.
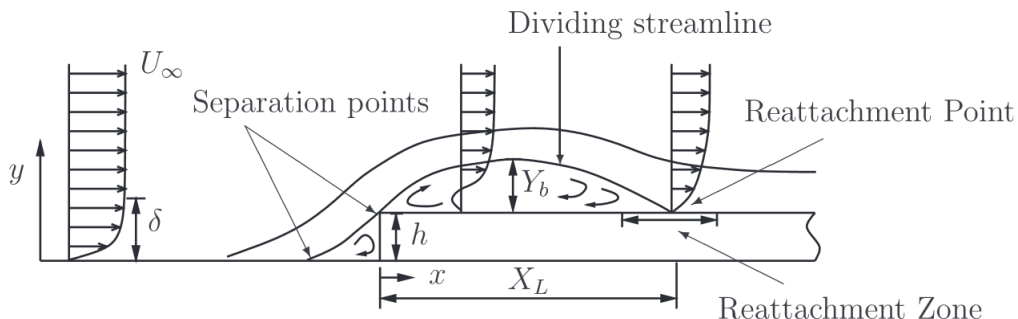
Figure 1.4: The flow features of the FFS flow; as illustrated by Sherry et al. (2010). The incoming boundary layer separates upstream of the step face with a upstream recirculation region forming. A separated shear layer is formed at the step edge with only one recirculation region rotating clockwise below a separated shear layer.

The flow separates from the step edge creating a strong shear layer between the reverse flow of the recirculation region and the freestream. Kelvin-Helmholtz (K-H) vortices develop in the separated shear layer. As the shear layer develops, the K-H vortices convect downstream and eventually merge, which increases local flow mixing and turbulent intensity. Compared with the separated shear layer in the BFS flow, the separated shear layer in the FFS flow deflects into the freestream, curves down to the bottom wall and reattaches. As discussed by Sherry et al. (2010), the FFS flow resembles the blunt flat plate when the boundary layer thickness to step height ratio $\delta/h << 1$. For a blunt flat plate, it was found by Kiya and Sasaki (1983) that 'regular' vortices are shed in the separation region with a frequency of 0.6 Hz. This 'regular' shedding vortices accumulates vorticity within the recirculation region. This accumulation leads to a large increase of the recirculation length. The accumulated vortices eventually shed down as a large vortex with a lower frequency of 0.2 Hz and suddenly reduces the recirculation length to a great extent.

1.3.3 Flow over a surface-mounted fence

Further flow complexity occurs when the separated shear layer as shown in Figure 1.4 does not reattach to the top surface of the obstacle as shown in Figure 1.2. When the ratio of the obstacle height to length is small, the flow is considered a SMF. The mean flow topology over a SMF was described in section 1.2. The boundary layer separates upstream of the fence at approximately $-0.65 < x_f/h < -0.55$ at $Re_h = 10\,500$; as discussed by Siller and Fernholz (2007) and Orellano and Wengle (2000). However, the upstream separation point will be a function of the inlet boundary layer profile and the δ/h ratio. The extent of upstream influence of the fence on the pressure field increases with increasing δ/h; as discussed by Good and Joubert (1968) and Castro and Fackrell (1978). The flow reattaches to the upstream face of the fence before separating from the primary separation point at the fence leading edge. The flow accelerates over the fence due to mass conservation and an intense shear layer develops between the freestream flow and the recirculation region behind the fence.

The flow reattaches downstream at the mean reattachment point, X_r, which is a function of the parameters shown in Equation 1.3.

$$X_r/h = f\left(\delta/h, Re_h, H/h, B/h, Tu\right), \tag{1.3}$$

where H/h and B/h are the height (H is the depth of the water channel) and width (B is the width of the water channel) aspect ratios respectively and Tu is the freestream turbulence intensity. Huppertz and Fernholz (2002) also showed the reattachment position is dependent on the fence sweep angle α but only flow normal to the fence as shown in Figure 1.2 was considered in this investigation.

However, the recirculation region is unsteady and the reattachment point oscillates in a reattachment zone as shown in Figure 1.2. Further, within the primary recirculation region, a secondary recirculation region occurs adjacent to the downstream face of the fence due to

the induced flow by the primary recirculation region. The separation point of the secondary recirculation region occurs at approximately $X_s/h = 1.60$; as discussed by Siller and Fernholz (1997) and Orellano and Wengle (2000). Prior research has focused on the drag experienced by SMF's in turbulent boundary layers (Good and Joubert, 1968; Castro and Fackrell, 1978) and reducing X_r via active manipulation of the two instability mechanisms which affect the SMF flow field (Orellano and Wengle, 2000, 2001; Siller and Fernholz, 1997, 2007; Huppertz and Fernholz, 2002; Choi and Kim, 2010).

The above separating and reattaching flows are susceptible to two instabilities: the K-H instability of the shear layer and a 'shedding-type' instability of the whole recirculation region. It was discussed by Sigurdson (1995a) that the two instability modes are different but not uncoupled. The basic difference is that the K-H vortices interacts with itself in the free shear layer and the 'shedding-type' instability results from the interaction of the vorticity with the wall.

The K-H instability has been investigated in various flow geometries. In the 2D simulation study of a BFS by Neto et al. (1993), it was found using vorticity contours that the dynamic flow structures were similar to that in a free mixing layer. The shedding and pairing of K-H vortices were also observed in a high Reynolds number mixing layer study by Winant and Browand (1974). In their study, a free mixing layer was generated using two water streams of different velocity. The dye visualisation revealed that the unstable waves grow and the fluid is observed to roll up into discrete vortices. These vortical structures interact with each other and merge with a single vortical structure forming which is approximately twice the spatial length of the former vortices. Browand (1966) also found the sub-harmonic frequencies related to the vortex pairing events. The scaling of the K-H frequency for a blunt flat plate was discussed by Sigurdson (1995a) using the result of Freymuth (1966). Based on the study of Freymuth (1966), the K-H frequency was non-dimensionalised in the Strouhal

number St_θ, which was defined in Equation 1.4:

$$St_\theta = f_{K-H}\theta/U_c,\tag{1.4}$$

where f_{K-H} is the K-H frequency, θ is the momentum thickness at the separation point and U_c is the convection velocity at the separation point. Freymuth (1966) discussed that the St_θ is constant.
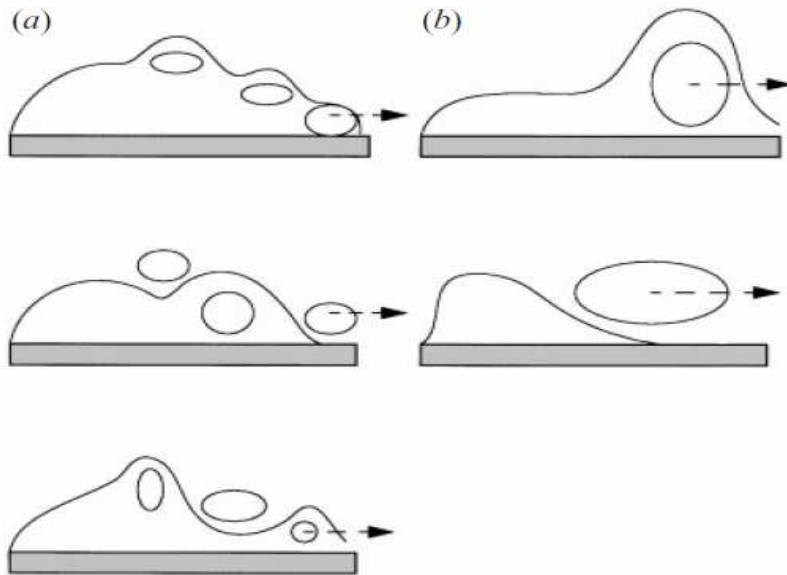
Figure 1.5: Two different types of shedding instability. The left column shows the topological structures of the normal shedding. The right column shows the topological shedding structures that impact the low frequency instability; as shown by Yang and Voke (2001)

The 'shedding type' instability was investigated experimentally by Sigurdson (1995b) and numerically by Yang and Voke (2001). The term 'shedding-type' instability was first used by Sigurdson (1995b) who found the low frequency large scale vortex shedding from the recirculation region of several bluff bodies could be described by a universal Strouhal number. Based on the study of Sigurdson (1995b), a universal Strouhal number exists for the 'shedding type' instability. This universal Strouhal number (St_{shed}) is defined in

Equation 1.5:

$$St_{shed} = f_{shed} Y_b / U_s, \tag{1.5}$$

where f_{shed} is the shedding frequency of large scale vortex structures from the recirculation region, Y_b is the maximum height of the recirculation region and U_s is the velocity at separation. It was found that St_{shed} has a constant value of 0.08 ± 0.01. In the numerical study of a flat plate by Yang and Voke (2001), two shedding topologies were discussed, as shown in Figure 1.5. Figure 1.5(a) represents the shedding of the small vortices. The shedding of these small vortices does not have a great impact on the recirculation region, although the instantaneous reattachment point will change accordingly. Figure 1.5(b) shows another vortex-shedding topology. In this large-vortex-shedding topology, several small vortices form a larger structure and eventually a relatively large vortex structure collapses and sheds downstream. This type of shedding mechanism has a large impact on the recirculation region and the instantaneous reattachment length will be shorter after a large scale vortex is shed compared with the shedding of the small vortices in Figure 1.5(a). Yang and Voke (2001) confirmed that the instantaneous reattachment length reduces to a much lower value when a large scale structure is shed downstream.

Since the separating-reattaching flow contains two instabilities, two frequencies have been used to manipulate the flow. In manipulated turbulent boundary layer flow over a SMF, Siller and Fernholz (2007) and Orellano and Wengle (2000) showed that both high-frequency and low-frequency forcing can reduce X_r. The high-frequency forcing influences the K-H instability whereas the low-frequency forcing influences the 'shedding-type' instability. The Strouhal number St_h is scaled as $St_h = fh/U_\infty$ (f is the forcing frequency in manipulated flow). The largest reduction in X_r was achieved by influencing the entire recirculation region (Siller and Fernholz, 2007; Orellano and Wengle, 2000). In the study of Orellano and Wengle (2000), the manipulation was conducted by fluid injection from a slot located upstream of the fence with two forcing frequencies ($St_h = 0.6$ and $St_h = 0.08$) at $Re_h = 3\,000$.

It was found that the X_r reduces by 10% when the high-frequency forcing Strouhal number ($St_h = 0.6$) was employed. However, the mean reattachment length was reduced by 36% when the low-frequency forcing Strouhal number ($St_h = 0.08$) was used. In the study of (Siller and Fernholz, 1996), the reverse-flow region upstream and downstream of a fence was investigated with manipulation of $Re_h = 10\,500$. The optimal frequency was found to be the natural shedding frequency downstream of the reattachment point. It was found from the instantaneous velocity field that a vortex forms at the disturbance slot upstream of the fence. This vortex convects towards the fence and flows over it. The time-mean recirculation region downstream of the fence was reduced by 40% when a disturbance is induced in front of the upstream recirculation region.

It is known that the δ/h ratio can affect the reattachment length through the following mechanisms. When $\delta/h < 1$, the free stream velocity will interact with the fence edge directly, *i.e.* the velocity at separation equals the freestream velocity, $U_s \approx U_\infty$. When $\delta/h > 1$, the velocity at separation is less than the freestream, $U_s < U_\infty$; therefore, a larger perturbation and greater flow deflection into the freestream will occur for the $\delta/h < 1$ case (Sherry et al., 2010).

1.3.4 Hypothesis

Based on the critical literature review presented, the parameters that affect the reattachment length behind a SMF were presented in Equation 1.3. Based on the topology of the instability shown in Figure 1.5, the 'shedding-type' instability affect the reattachment length of the separated shear layer. The 'shedding-type' structure is formed by amalgamation of the K-H vortices. Therefore, it is hypothesized that the parameters which affect X_r, also influence the instability mechanisms. Specifically, different δ/h ratios will affect the flow downstream of the fence by changing the velocity at the separation point. The velocity at the separation point determines the amount of perturbations in the separated shear layer. This is analogous to the flow over mountainous terrain, where the velocity interacting with the mountain ridge

will vary due to thermal effects in the atmospheric boundary layer. This hypothesis is investigated by holding Re_h constant and varying the δ/h ratio.

Chapter 2

Experimental Setup

This chapter describes the experimental methods used for the acquisition of my measurements, which includes the water channel and PIV (Particle Image Velocimetry) setups.

2.1 Water Channel

The measurements were performed in a closed-circuit, open surface water channel at the University of Calgary as shown in Figure 2.1. Water is first pumped from the return line into a main plenum and then through a honeycomb, achieving uniformed flow, before passing through a 6:1 contracted acceleration section. The working section within the glass water channel whereupon optical measurements were obtained was $385 \times 430 \times 4125$ mm that immediately followed the acceleration section. The test section ends at a reservoir, which circulates water back via an axial pump. A heater was applied to the circulating fluid to develop boundary layers of different thickness while maintaining matching Re_h. At the junction of the contraction and first test sections at a distance of $79.29h_{min}$ upstream from the fence, a 2mm-diameter rod was placed on the bottom wall of the water channel to ensure that a turbulent boundary layer developed at the fence position. Here, h_{min} represents the small fence height of 20 mm.

A plenum
B conditioning units
C 6:1 contraction
D boundary layer development section
E measurement section
F traverse
G Photron SA4 camera
H laser
I recirculation chamber
J returning pipe and pump
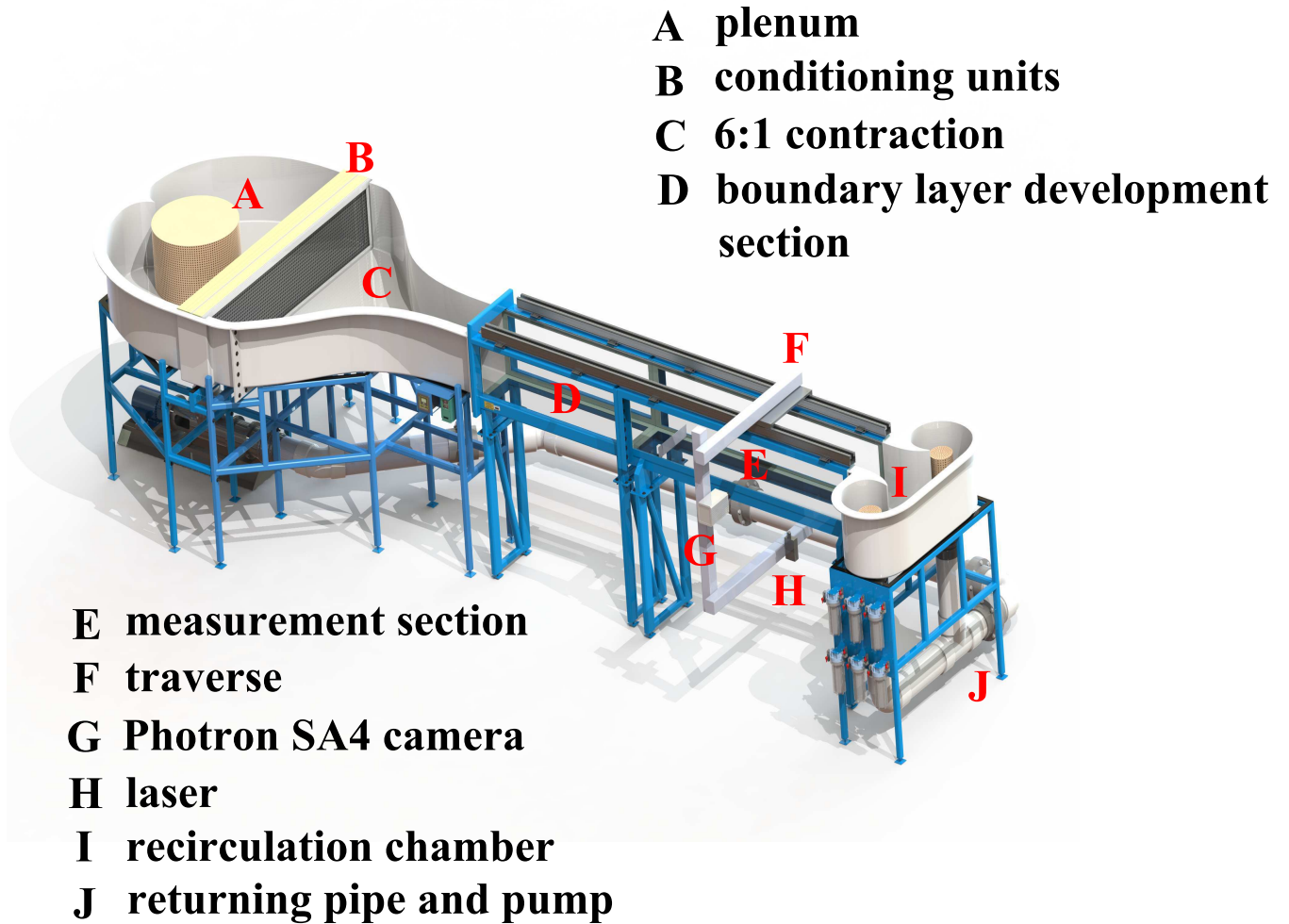
Figure 2.1: Schematic of the closed-circuit water channel facility.

2.2 PIV Measurements

The PIV system, as shown in Figure 2.2, consists of a 532 nm, 1 Watt continuous wave solid state laser (Dragon lasers, Changchun, Jilin, China), and a high-speed SA-4 camera (Photron, San Diego, CA, USA) with a maximum resolution of 1024×1024 pixels.
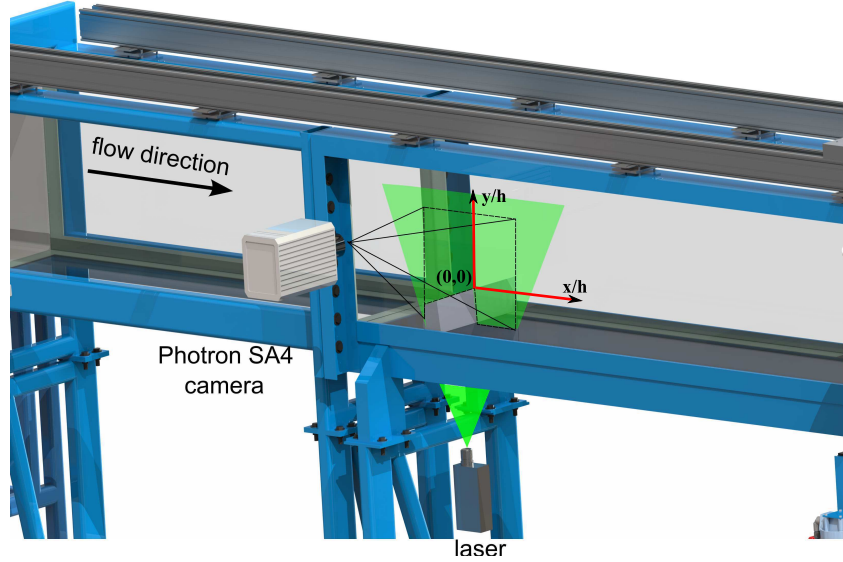
Figure 2.2: Schematic diagram presenting the PIV setup used to acquire 2D velocity fields.

The time-resolved PIV images were taken in the xy-plane, where the coordinate was defined as the fence upstream separation point. The PIV measurement in these two cases were not completely time-resolved for all sizes of eddies. However, in this current measurement only K-H instability in the departing shear layer and the 'shedding-type' structure are interested. The frame rate of the camera was chosen for enough measurement time to resolve the K-H vortices and the 'shedding-type' structure. For the thin boundary layer case, images were acquired at a resolution of 704×1024 pixels and at a frame rate of 125 frame-per-second (fps). For the thicker boundary layer case, images were acquired at a resolution of 1024×1024 pixels and at a frame rate of 500 fps. In order to measure the entire flow field, starting from the fence position to positions further downstream of the reattachment point, the camera and laser were mounted on a traverse that allowed for concurrent movement whereupon measurements were acquired in multiple downstream windows shown in Figure 2.3. Seeding particles in the form of silver coated hollow glass spheres with a mean diameter of 100 um were added to the flow (Potters Industries, Malvern, Pa, USA). These seeding particles presented with a Stokes number (Stk) of approximately 2.4×10^{-3}, which

16

suggests they faithfully followed the circulating fluid. The Stk is defined as Equation 2.1:

$$Stk = \frac{\tau_p}{\tau},\tag{2.1}$$

where τ_p is the relaxation time of the seeding particle and τ is the characteristic time scale of the flow. The relaxation time (τ_p) can be expressed as: $\tau_p = u_s/g$, where u_s is the settling time of the particle and g is the gravitational acceleration. The measurement uncertainty is 49.89 mm/s at a confidence of 95% in the thin-boundary-layer case. Further details of measurement uncertainly are presented in Appendix A.
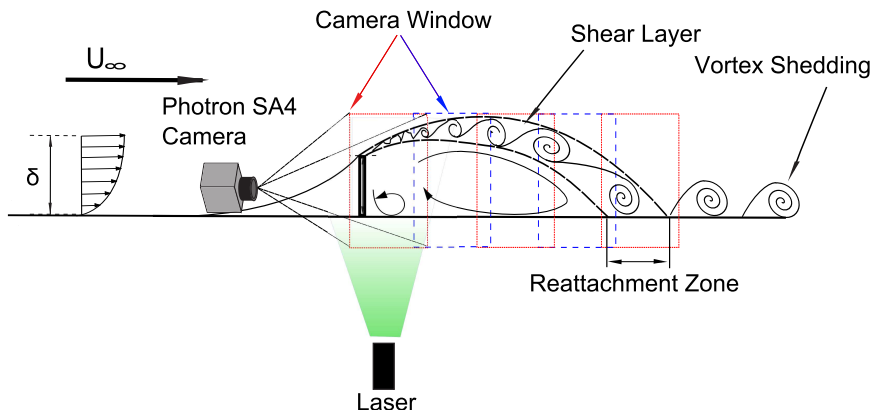
Figure 2.3: Schematic representation of the PIV flow field. The camera moved simultaneously with the laser, recording multiple-windows of the separated flow field.

2.3 Incoming Boundary layer

The incoming boundary layers were first measured before measuring the wake flow of the SMF. The incoming boundary layer of the two cases was measured at the fence position (1.9 m from the inlet of section D of Figure 2.1) in absence of the fence in the experimental setup. The boundary layer profiles are shown in Figure 2.4 as a function of y/h and in Figure 2.5 as a function of y/δ, where y is the vertical distance from the bottom wall of the water channel and δ is the boundary layer thickness from the bottom wall of the water

17

channel. Figure 2.4 shows the scaling of the BL thickness to the fence height in the two BL cases. Figure 2.5 shows that the profiles of the BL were planned to be close between the two cases.
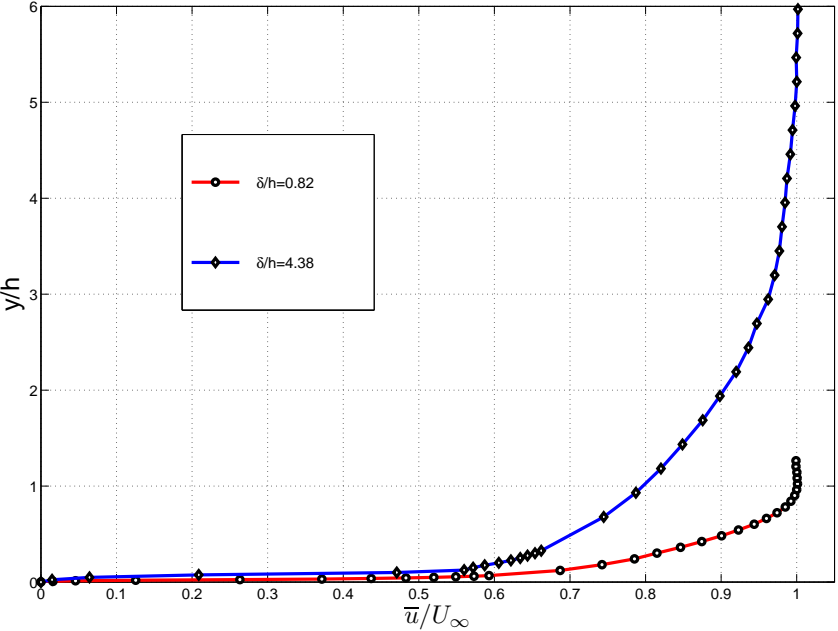
Figure 2.4: Normalized thin and thick boundary layer profiles as a function of y/h measured at the fence position in absent of the fence, where is 1.9 m from the wiring trip. The red line represents the thin boundary layer case while the blue represents the thick boundary layer case. Both boundary layer profiles are normalised by each individual free-stream velocity and fence height to show the scale of the BL to fence height ratio.
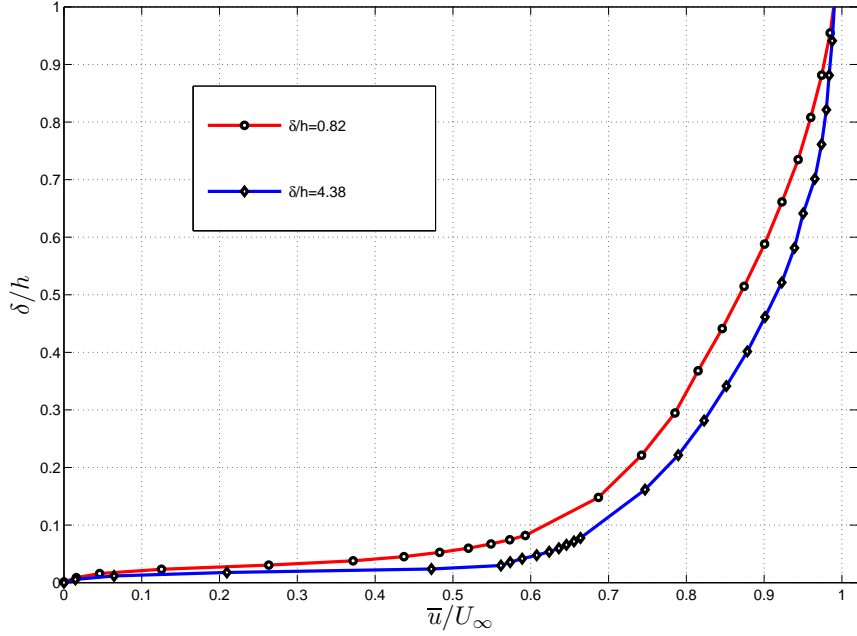
Figure 2.5: Normalized thin and thick boundary layer profiles presented as a function of y/δ. From this figure, it can be seen that the profile shape of both the thin boundary layer and the thick boundary layer are similar.

In order to achieve different δ/h, a heater was applied to change the viscosity that necessitated an alteration of the inlet freestream velocity that allowed for the maintenance of matching Re_h as shown in Table 2.1. Boundary layer profiles were maintained to be similar as shown in the similar value of the shape factor $(H^\star)$ between the two boundary layer cases and Figure 2.5. The shape factor $(H^\star)$ is calculated as $H^\star = \frac{\delta^*}{\theta}$. δ^* is the displacement thickness of the boundary layer defined in Equation 2.2. θ is the momentum thickness of the boundary layer defined in Equation 2.3.

$$\delta^* = \int_0^\delta (1 - \frac{\overline{u(y)}}{U_\infty})dy, \tag{2.2}$$

$$\theta = \int_0^\delta \frac{\overline{u(y)}}{U_\infty}(1 - \frac{\overline{u(y)}}{U_\infty})dy, \tag{2.3}$$

19

where $\overline{u(y)}$ is the time-averaged streamwise velocity in function of vertical position. Detailed information regarding the incoming boundary layer of both cases are summarized in Table 2.1

Table 2.1: Experimental parameter values in accordance with the thin and thick boundary layer (BL) conditions

Parameters	Units	Thin BL	Thick BL
Fence height h	m	0.090	0.021
Free-stream velocity U_∞	ms^{-1}	0.10	0.33
Water Temperature T	°C	25.9	38.4
Kinematic Viscosity ν	m^2s^{-1}	8.54×10^{-7}	6.60×10^{-7}
Reynolds number Re_h		10539	10497
Distance between inlet and fence x	m	1.90	1.90
Boundary layer thickness δ	m	0.074	0.092
Boundary layer thickness δ/h		0.82	4.38
Displacement thickness δ^*	m	0.013	0.013
Momentum thickness θ	m	8.38×10^{-3}	8.36×10^{-3}
*Shape factor $H^\star$		1.6	1.5

Note: *Shape factors show that the profile shapes are similar.

Chapter 3

Results and Discussions

This chapter describes both the time-averaged and the unsteady features of the SMF flow. The time-averaged results will be analysed using the velocity, out-of-plane vorticity and turbulent intensity fields. The time-dependent nature of the SMF flow is discussed by analysing the frequencies present after completion of a Fast Fourier Transform (FFT) analysis. The time-dependent analysis is undertaken to determine how the vortices develop downstream of the SMF. The time-averaged flow features are presented first followed by the unsteady analysis.

3.1 Time Mean Results

In the following section, the time-averaged results including the velocity, vorticity and turbulent intensity will be investigated and discussed.

3.1.1 Velocity Field

Figure 3.1 shows contour maps of the time-averaged streamwise velocity, $\overline{u}/U_\infty$ and flow fields of both the thin and the thick BL cases. The thin BL case is shown at the top of Figure 3.1, whereas the thick BL case is shown at the bottom. The length and velocity scales of each case are normalised by its appropriate fence height and freestream velocity.
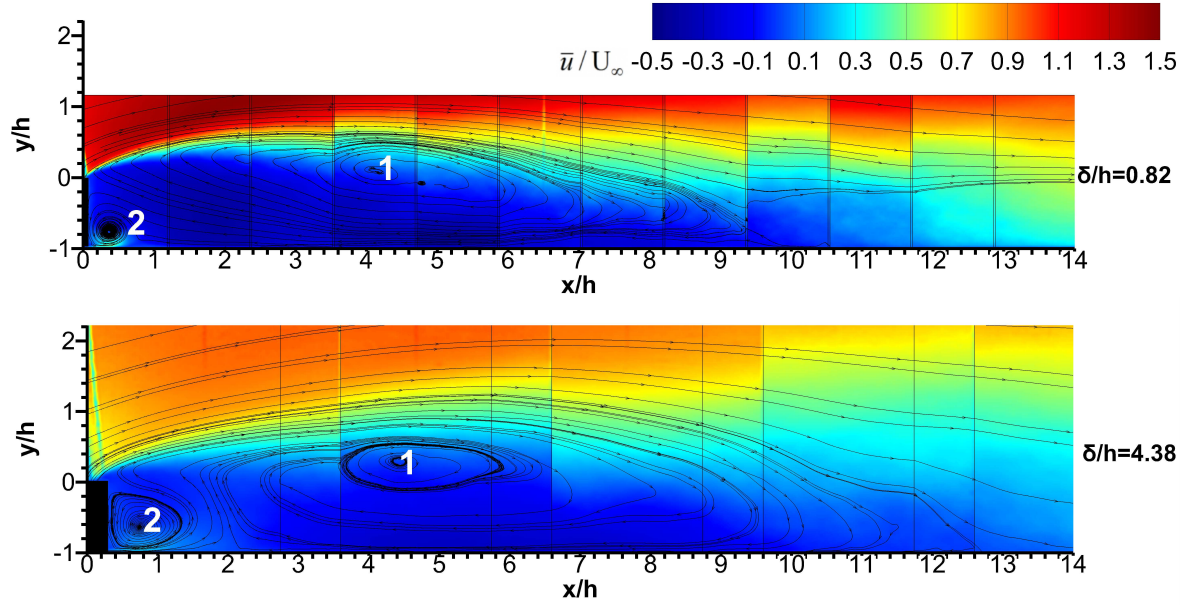
Figure 3.1: Contour maps of the non-dimensionalised time-averaged streamwise velocity, $\bar{u}/U_\infty$ and flow fields for the thin BL case (upper) and thick BL case (lower). Numbers 1 and 2 label the primary and the secondary recirculation regions respectively. The streamlines show that the reattachment length of the thick BL case is longer than that in the thin BL case.

The freestream flow is from left to right. Figure 3.1 reveals that a shear layer starts at the leading edge of the fence and grows wider until it reaches the bottom wall of the water channel. The shear layer growth is a possible proxy for the growth of vortices which form in the shear layer. Two recirculation regions form underneath the shear layer. The smaller recirculation region adjacent to the fence is denoted as the secondary recirculation region and rotates anticlockwise. The larger recirculation region is denoted as the primary recirculation region and rotates in a clockwise motion. Several statistics characterising the time-averaged recirculation regions are summarized in Table 3.1.

The reattachment point, X_r, can be defined as the point where one branch of the dividing streamline returns upstream into the recirculation region and the other continues in the downstream direction (Sherry et al., 2010). Alternatively, the separation or the reattachment

point of the flow occurs where the reverse flow parameter at the wall, χ_ω, attains a value of 50%, *i.e.* $\chi_\omega = 50\%$ (Siller and Fernholz, 1996). Here, the reattachment point of the shear layer and the length of the secondary separation region are determined by finding $\chi_\omega = 50\%$ close to the bottom wall ($y = 0.02h$ above the wall in the thick BL case and $y = 0.05h$ above the wall in the thin BL case). The reattachment length of the thin BL case is $X_r = 10.67h$ and that of the thick BL case is $X_r = 12.76h$. The difference of X_r between the two cases can be attributed to several factors. The first is the different velocities at the fence separation point (U_s). Since δ/h is different between the two BL cases, the velocity at fence separation point is $U_s/U_\infty = 73\%$ in the thin BL case and $U_s/U_\infty = 34\%$ in the thick BL case. Sherry et al. (2010) found for a FFS that a higher velocity interacts with the FFS edge and causes a higher perturbation. In the SMF study by Orellano and Wengle (2000), the reattachment length reduced when a forcing induces perturbation in the manipulated flow compared with non-manipulated flow. Therefore, when a SMF is within a thin BL, a higher perturbation is expected due to a higher interacting velocity and shear layer reattaches more quickly.

Table 3.1: Statistics characterising the time-averaged recirculation region.

Parameters	Thin BL	Thick BL
Length of primary recirculation region	$10.67h$	$12.76h$
Height of primary recirculation region	$1.8h$	$2.3h$
Length of secondary recirculation region	$0.88h$	$1.65h$
Height of secondary recirculation region	$0.6h$	$0.8h$

The reattachment lengths found in the two δ/h cases investigated here are shorter than the experimental results by Siller and Fernholz (1996) ($X_r/h = 13.60$) and the numerical computations by Orellano and Wengle (2000) ($X_r/h = 13.45$) at the same $Re_h = 10\,500$. Although the Re_h fluctuates around $Re_h = 10\,500$ in both the thin and thick BL cases ($Re_h = 10\,539$ and $Re_h = 10\,497$ respectively), this should not have a large affect on the

reattachment length. Siller and Fernholz (1996) found the reattachment length behind a SMF to be constant within their experimental uncertainty for $Re_h > 8\,400$. Sherry et al. (2010) also found a reduced dependency of X_r on Re_h for $Re_h > 8\,500$ for a FFS.

The height of the primary recirculation region is also different between the two cases, as shown in Figure 3.1. The height of the primary recirculation region can be approximated as the height of the upper boundary of the separating shear layer. The heights of the primary recirculation region for the thin and thick BL cases were around $1.8h$ and $2.4h$ respectively. The higher recirculation region in the thick BL is possibly due to a higher pressure in the primary recirculation region of the thick BL case.

In Figure 3.1, the secondary recirculation region shows a anticlockwise rotation. The secondary recirculation region forms in an analogous manner as the upstream recirculation region. When the reverse flow in the recirculation region travels back upstream toward the fence, boundary layer separation will occur due to the blockage by the fence. A stronger reverse flow will separate further downstream of the fence, creating a larger secondary recirculation region. The size of the secondary recirculation region is different between the two cases. The results of the thick BL case indicate a larger secondary recirculation region with a length and height of $1.65h$ and $0.80h$ compared to $0.88h$ in length and $0.60h$ in height for the thin BL case. It should be noted that a small gap (0.8 mm) between the fence bottom and the channel floor that was difficult to observe visually was discovered during the data processing. Such a gap allowed a velocity jet to form which likely disturbed the secondary recirculation region. As the velocity jet was in the direction of the anti-clockwise rotation of the secondary recirculation region, boundary layer separation will occur further downstream elongating the secondary recirculation region. The magnitude of the velocity jet could not be evaluated with the spatial resolution employed with the thick BL case.

As shown in Figure 1.2, the flow over a SMF also produces a further recirculation region upstream of the fence. Figure 3.2 shows the non-dimensionalised streamwise velocity fields

upstream of the fence for the $\delta/h = 0.82$ (left) and $\delta/h = 4.38$ (right) cases.
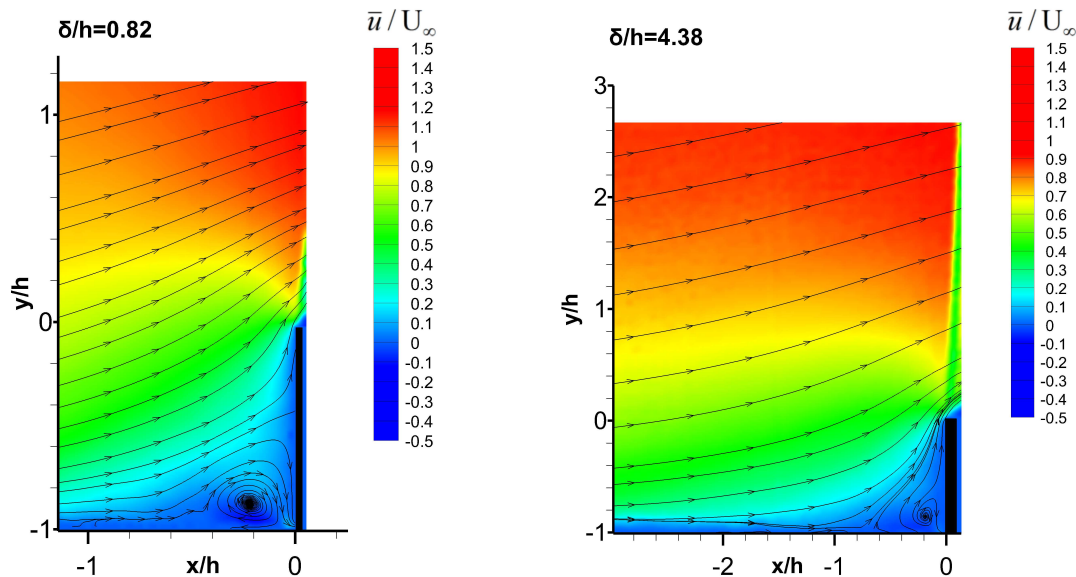
Figure 3.2: Contour maps of the non-dimensionalised time-averaged streamwise velocity flow field upstream of the fence for the thin BL case (left) and the thick BL case (right). Flow is from left to right. In the thin BL case, boundary layer separation occurs at $X_u = -0.6h$ whereas it occurs at $X_u = -0.7h$ for the thick BL case.

The flow is from left to right. The boundary layer separates around $0.6h$ upstream from the fence in both cases. A recirculation region is formed underneath the separated boundary layer and rotates in a clockwise direction. From the streamlines of the thin BL case, it can be clearly seen that the separated boundary layer reattaches on the front face of the fence. At this reattachment region, one branch of fluid flows vertically up along the surface of the fence and the other branch of fluid flows down to form the recirculation region. The fluid that flows vertically to the fence edge will interact strongly with the fluid at the fence edge. This interaction will cause a strong velocity deflection and further a strong vertical velocity gradient at the fence edge. Comparing the two cases in Figure 3.2, it can be seen that a larger amount of fluid flows vertically from this reattachment region to the fence edge in the thin BL case due to a higher fence blockage. Therefore, a higher vertical velocity gradient is

expected at the fence edge in the thin BL case. Velocity gradients at selected points near the fence edge are presented in Table 3.2. Velocity gradient components are normalised by their appropriate U_∞ and h. From Table 3.2, it can be seen that the vertical velocity gradient near the separation point is larger in the thin BL case. This larger vertical velocity gradient can be expected to generate a larger vorticity magnitude in the separated shear layer as will be discussed further in the following section.

Table 3.2: Velocity gradients near the separation point normalised by each U_∞ and h

	Thin boundary layer case	Thick boundary layer case
Velocity gradient	$(x = 0.054h, \ y = 0.050h)$	$(x = 0.146h, \ y = 0.076h)$
$\frac{\partial \overline{u}}{\partial x} \times \frac{h}{U_\infty}$	-8.03	-2.39
$\frac{\partial \overline{u}}{\partial y} \times \frac{h}{U_\infty}$	11.53	6.84
$\frac{\partial \overline{v}}{\partial x} \times \frac{h}{U_\infty}$	18.5	4.0
$\frac{\partial \overline{v}}{\partial y} \times \frac{h}{U_\infty}$	15.78	6.46

To characterise the trajectory of the separated shear layer, the height of the shear layer was calculated using Equation 3.1. The point of the separating shear layer trajectory is found at the vertical position where the time-averaged streamwise velocity equals to the maximum velocity difference; see Equation 3.1.

$$y_{sl}(x/h) = y(\overline{u(x/h)/U_\infty} = \Delta\overline{u(x/h)/U_\infty}/2), \tag{3.1}$$

where $\Delta\overline{u(x/h)/U_\infty} = \overline{u(x/h)/U_\infty}_{max} - \overline{u(x/h)/U_\infty}_{min}$ is the maximum velocity difference across the shear layer. $\overline{u(x/h)/U_\infty}_{max}$ is the maximum streamwise velocity at each horizontal point. $\overline{u(x/h)/U_\infty}_{min}$ is the minimum streamwise velocity at each horizontal point. Figure 3.3 shows the trajectory, $y_{sl}(x/h)$, of the separated shear layer of both BL cases.
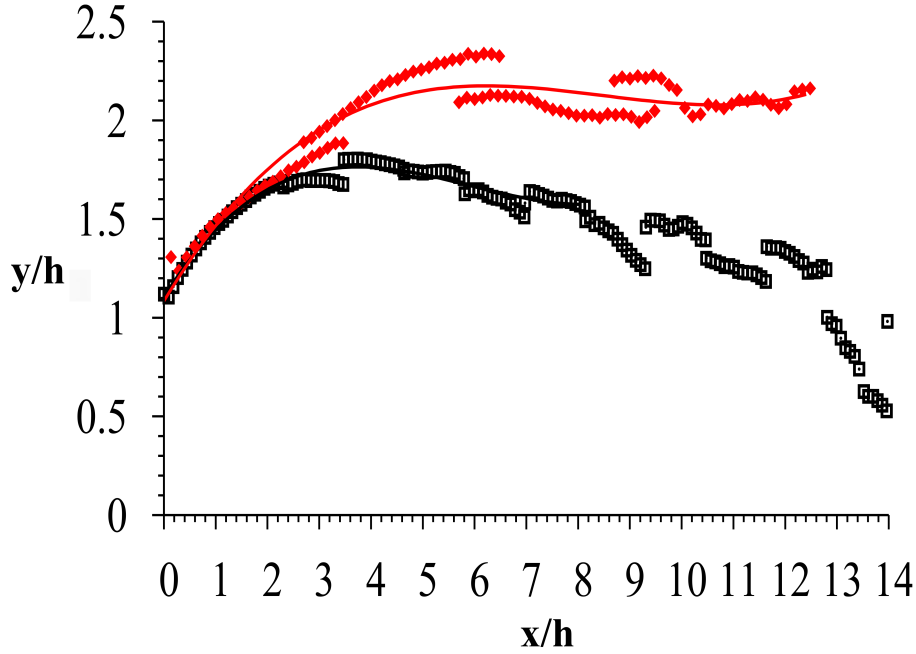
Figure 3.3: Comparison of the shear layer trajectory between the two boundary layer cases. The red curve represents the trajectory of the thick BL case and the black curve represents the trajectory of the thin BL case.

The black and red lines represent the thin and thick BL cases respectively. Close to separation $(0 < x/h < 1.5)$, the trajectories of the separated shear layer are very similar due to bluff body geometry effects. However, for $x/h > 1.6h$, the thin BL trajectory is lower than the thick BL case. This is likely due to a field of view restriction above the fence in the thin BL case which will result in a lower $\Delta \bar{u}/U_\infty$ and hence suppression of $y_{sl}(x/h)$.

3.1.2 Vorticity Field

To further characterise the separated shear layer, the spanwise vorticity field was calculated using Equation 3.2,

$$\overline{\omega}_z = \frac{\partial v}{\partial x} - \frac{\partial u}{\partial y}, \tag{3.2}$$

where v is the vertical velocity component.

Figure 3.4 presents the time-averaged non-dimensionalised spanwise vorticity field for the $\delta/h = 0.82$ (upper) and $\delta/h = 4.38$ (lower) cases. It shows the vorticity magnitude is largest at the separation point where vortex formation initializes. It then diffuses quickly at around $x = 3 - 4h$. When comparing the non-dimensionalised vorticity in the shear layer between the thin and thick BL cases, the thin BL case has a higher magnitude. This can be explained by the different amount of BL vorticity available to the separated shear layer in each case. As shown in Equation 3.2, vorticity is defined by the product of the velocity gradients, $\frac{\partial v}{\partial x} - \frac{\partial u}{\partial y}$. The vorticity level within a boundary layer is obviously higher than in the freestream where no such velocity gradients are present. Therefore, in the thin BL case, it is expected that a larger percentage of the boundary layer vorticity will contribute to that in the separated shear layer compared to the thick BL case. With a δ/h ratio less than unity and the freestream velocity interacting with the SMF edge, the separating shear layer is deflected further into the freestream (Sherry et al., 2010). The vorticity in a separated shear layer which is deflected further into the freestream will be larger than a less deflected shear layer due to the streamwise velocity gradient in the y-direction, *i.e.* $\frac{\partial u}{\partial y}$. As shown in Table 3.2, the non-dimensionalised velocity gradient equals $\frac{\partial u}{\partial y} \times \frac{h}{U_\infty} = 6.84$ in the thick BL case and $\frac{\partial u}{\partial y} \times \frac{h}{U_\infty} = 18.5$ in the thin BL case. For these reasons, the non-dimensionalised spanwise vorticity, $\overline{\omega}_z h/U_\infty$, is greater in the thin BL case.

Further, Figure 3.4 indicates that the vorticity in the shear layer diffuses quicker in the thick BL case compared to the thin BL case. In a viscous fluid, vorticity is primarily diffused

by two mechanisms, viscous and turbulent diffusion. The Re_h in the two δ/h cases is the same so the viscous component of vorticity diffusion can be expected to be similar. Therefore, turbulent diffusion must play a larger role in the thick BL case. Turbulent diffusion can be gaged by the turbulence intensity levels above the SMF. The turbulent intensity within a turbulent boundary layer is higher than that in the freestream. Therefore, in the thick BL case, where the separation point at the fence edge is submerged within the turbulent boundary layer, turbulence effects will play a role immediately. Hence, in the thick BL case, a more turbulent flow at separation will cause a greater amount of mixing between the irrotational freestream and the recirculation region leading to more rapid vorticity diffusion. In the thin BL case, the turbulence intensity in the freestream interacts with the separated shear layer resulting in less turbulent diffusion of vorticity. The turbulence intensity created by the SMF is discussed further in the following section.
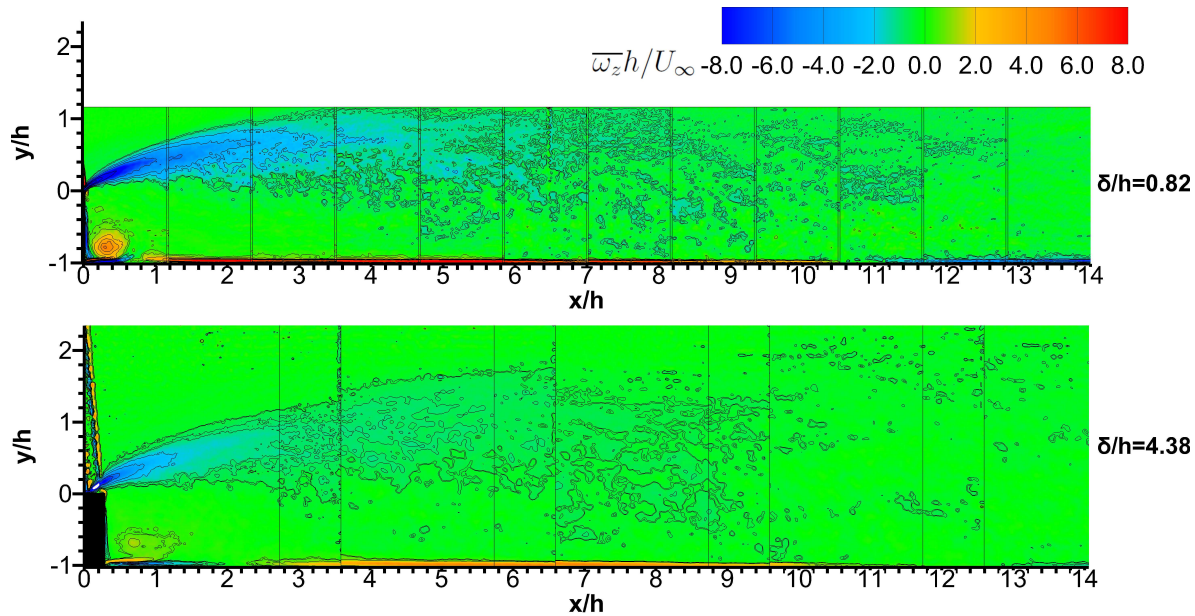
Figure 3.4: Contour map of the non-dimensionalised spanwise vorticity, $\overline{\omega_z}h/U_\infty$ for the $\delta/h = 0.82$ (upper) and $\delta/h = 4.38$ (lower) cases. The peak vorticity magnitude in the shear layer is largest in the thin BL case.

3.1.3 Turbulent Intensity Field

The vorticity field partially indicated the turbulent nature of the flow downstream of the SMF. To further characterise the turbulent nature of the SMF wake, the turbulence intensity was calculated using Equations 3.3 and 3.4.

$$Tu = u_{rms}/U_\infty, \tag{3.3}$$

$$u_{rms} = \sqrt{\frac{1}{2}(u'^2 + v'^2)}, \tag{3.4}$$

where Tu is the normalised turbulent intensity, and u_{rms} is the root-mean-square velocity calculated by from the streamwise (u') and vertical (v') velocity fluctuations. Since the velocity field was measured in a planar laser sheet, the fluctuating velocity component of u' and v' were determined and considered.
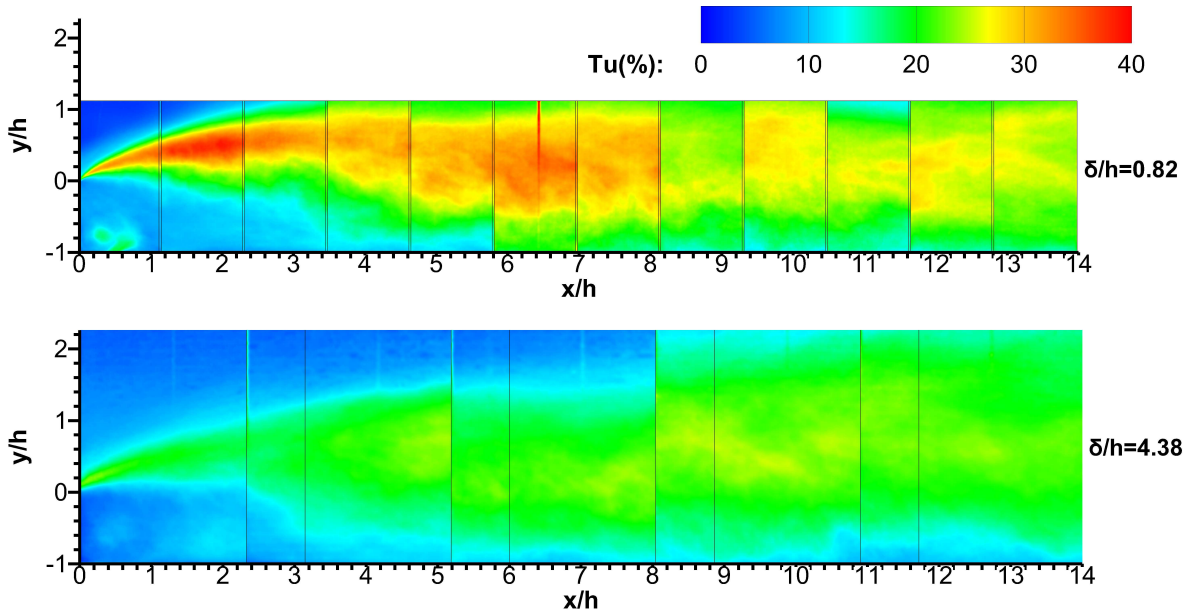
Figure 3.5: Contour maps of the non-dimensionalised turbulent intensity for the $\delta/h = 0.82$ (upper) and $\delta/h = 4.38$ (lower) cases. The magnitude of the shear layer turbulent intensity is higher in the thin BL case.

Figure 3.5 shows the time averaged turbulent intensity fields for the $\delta/h = 0.82$ (upper) and $\delta/h = 4.38$ (lower) cases. It is apparent that the turbulent intensity is larger in the thin BL case. Based on Boussinesq approximation, a higher velocity gradient will cause a higher Reynolds stress. Reynolds stress can indicate the turbulent intensity. Therefore, in the thin BL case, higher turbulent intensity is due to the higher velocity gradient at the fence separation point. Further, in the thick BL case, it can be seen that the turbulent intensity diffuses rapidly at around $x = 2.2h$. This could be because the vortices in the shear layer grow in size, increasing fluid entrainment across the shear layer. In the time-mean turbulent intensity field, a discontinuity of the contour maps is evident between each window. This is likely due to the limited measurement time for each window (63.5 seconds in the thin BL and 10.9 seconds in the thick BL). The measurement time was limited by the camera buffer capacity.

The mean turbulence intensity field revealed the turbulent nature of the SMF wake. To further investigate the time-dependent nature of the SMF, a unsteady analysis was undertaken and will be presented in the following section.

3.2 Unsteady analysis

The literature review revealed that two instability mechanisms affect the SMF wake, a K-H instability in the separated shear layer and a 'shedding-type' instability which affects the entire primary recirculation region. The two instability mechanisms will be addressed separately in the current section.

3.2.1 Kelvin-Helmholtz Instability

The K-H instability mode is a common feature of mixing and separated shear layers. To investigate the K-H mode in the separated shear layer, a Fast Fourier Transform (FFT) was calculated at each spatial point over the entire measurement time series to determine the

dominant frequencies. Figure 3.6 shows the results of the FFT analysis for the $\delta/h = 0.82$ case along the shear layer in the range $0 \leq x/h \leq 2.5$.
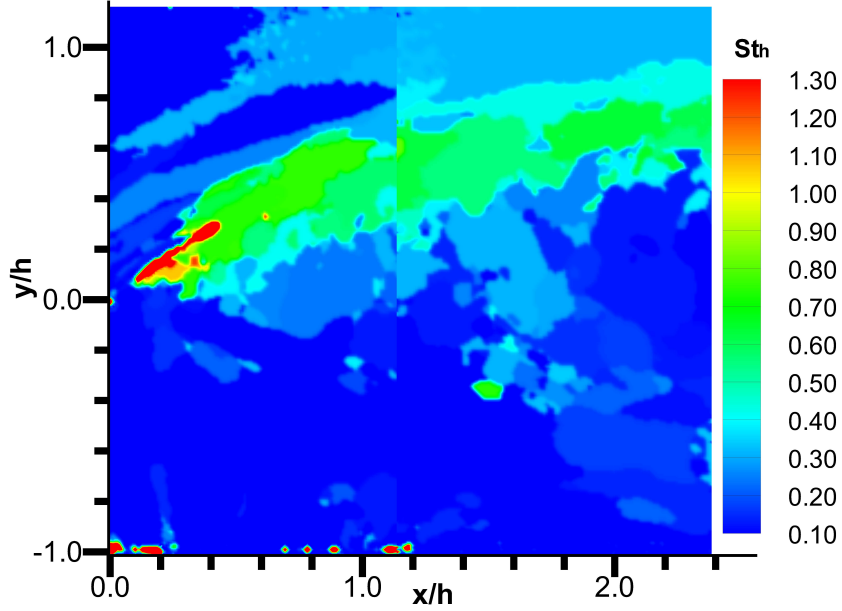
Figure 3.6: The development of the St_h along the shear layer for the $\delta/h = 0.82$ case in the range $0 \leq x/h \leq 2.5$. The frequencies are presented as the St_h, constructed from h and U_∞. The St_h is around 0.09 between $x = 0.02h$ and $x = 0.08h$. Then the St_h increases from 1.7 at $x = 0.11h$ to 4.8 at $x = 0.20h$ and decreases to 1.6 at $x = 0.42h$. At $x = 0.43h$, the St_h decreases to 0.83, which is approximately half of the St_h at $x = 0.42h$. The St_h further decreases to around 0.57 at $x = 0.88h$, which is around half of the St_h at $x = 0.43h$.

The frequency data is presented as a St_h ($St_h = f_{K-H}h/U_\infty$), where f_{K-H} is the frequency of the K-H instability. The St_h maintains a constant value of around 0.090 for $0.02 \leq x/h \leq 0.08$. This value corresponds to the high pass frequency filter limit applied to the data. It indicates the bluff body dominance of the SMF flow. The St_h then increases from 1.7 at $x = 0.11h$ to 4.8 at $x = 0.20h$. The St_h then decreases to 1.6 at around $x = 0.43h$. The fluctuation of the St_h is associated with the beginning of the K-H instability

mode. Based on the study of Orellano and Wengle (2000), in the separating shear layer when the St_h is transferred from a higher frequency to a lower frequency, a vortex pairing event occurred. For instance, in the study by Orellano and Wengle (2000), two vortex pairing events happened when St_h first decreased from 1.2 to 0.6 and further decreased to 0.3 along the separated shear layer. Therefore, following our analysis strictly in Figure 3.6, the first pairing event occurs when St_h reduces to 0.83 from 1.60. Then the St_h further decreases to around 0.57 at $x = 0.88h$, which is a likely indication of a secondary pairing event.

The results of Figure 3.6 are compared to those by Orellano and Wengle (2000) at $Re_h = 3\,000$ and $\delta/h = 0.8$. Their results showed an amplification of frequencies in the range $0.3 < St_h < 1.8$ at $x = 0.6h$. In non-manipulated SMF of Orellano and Wengle (2000), a peak St_h of 1.2 was found corresponding to the fundamental frequency of the primary roll-up of the separated shear layer. Between $x = 0.6h$ and $x = 2.0h$, energy was transferred to lower frequencies from $St_h = 1.2$ to $St_h = 0.6$ and then further to $St_h = 0.3$, indicating two vortex pairing events occurred before $x = 2.0h$ (Orellano and Wengle, 2000).

The K-H instability in the thin BL case shows a higher St_h than in the study of Orellano and Wengle (2000) at a similar δ/h value. Based on the study of Sigurdson (1995a), the St_θ of the K-H instability has a constant value. Since the δ/h was around 0.8 for both the thin BL case of the present study and that of Orellano and Wengle (2000), it could be expected that the momentum thickness (θ) at the separation point is similar. However, the width aspect ratio of the models is different between the two studies (6.75 in Orellano and Wengle (2000)). The current results are therefore likely to suffer more from three dimensional effects. Further, the inlet boundary layer profiles are not equivalent between the two investigations. Finally, the convection velocity at the separation point is different due to different Re_h. At higher Re_h, the velocity at the separation point is expected to be higher than in the lower Re_h case. Hence, the thin BL case is expected to have a higher K-H frequency (f_{K-H}). This higher K-H frequency leads to a higher St_h in the thin BL case.

Figure 3.7 shows the dominant frequencies along the shear layer for the $\delta/h = 4.38$ case in the range $0 \leq x/h \leq 6.5$.
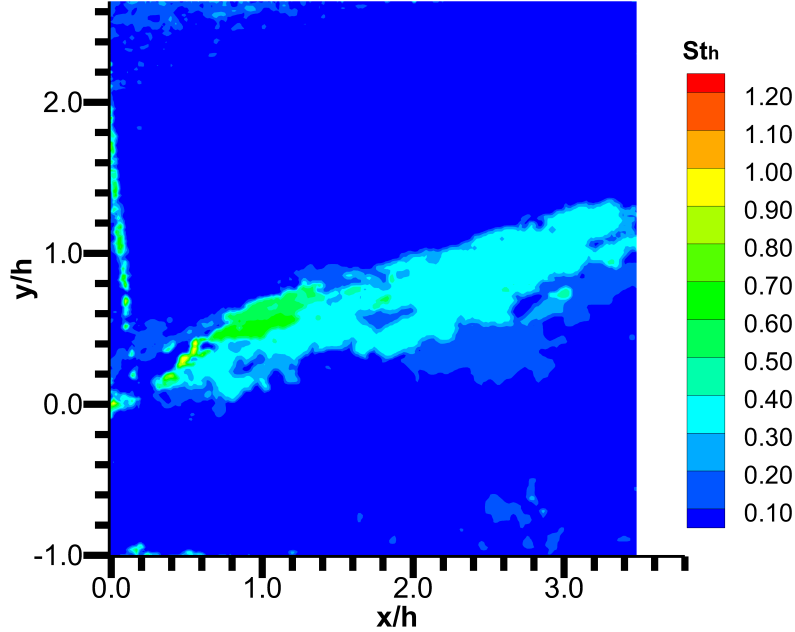
Figure 3.7: The development of the dominant Strouhal number (St_h) along the shear layer for the $\delta/h = 4.38$ case in the range $0 \leq x/h \leq 6.5$. The St_h decreases from around 0.81 at horizontal position of $x = 0.48h$ to 0.40 at horizontal position of $x = 1.2h$. This is due to the first vortex pairing event which causes a doubling of the period. A second decrease in the St_h occurs at around $x = 1.9h$, which decreases to 0.27. This is due to the second vortex pairing event. The vertical band above the fence was because of the laser refraction through the transparent fence.

Again, the frequencies are presented as the St_h. At a wake position around $x = 0.48h$, the St_h is around 0.81. At a wake position of $x = 1.2h$, the St_h decreases to 0.40, which is approximately half of that in position of $x = 0.48h$. This halving of the St_h is due to a vortex pairing event. Finally, at a wake position of $x = 1.9h$, the St_h decreases to 0.27, which is approximately half of that at $x = 1.2h$. Furthermore, based on the first location of

period doubling, the first vortex pairing event occurs around $x = 1.2h$. In a similar fashion, the second vortex paring event occurs at $x = 1.9h$.

Comparing the development of the vortex structures in the shear layer between the two cases, the St_h is higher in the thin BL case. The K-H instability frequency of the thin BL case is approximately twice that of the thick BL case. K-H instability can occur where there is a high level of velocity gradient in a single continuous fluid. Therefore, the higher velocity gradient at the fence separation point in the thick BL case (see Table 3.2) will cause a higher f_{K-H}, which will correspondingly lead to a higher St_h for the thick BL layer case.

The wake position where the first vortex pairing event occurs is also different between the two δ/h cases. In the thin BL case, the first and second pairing events occur closer to the separation point compared to the thick BL case. This is likely due to the three-dimensional effects caused by the different aspect ratios, B/h, in the two cases. Here, the aspect ratio was $B/h = 4.28$ for the thin BL case and $B/h = 18.3$ for the thick BL case. With a reduced B/h reduces, the two-dimensional region of the reattachment line on the bottom wall will be narrowed in the spanwise direction. This is due to the boundary layer from the side wall of the water channel.

3.2.2 'Shedding-type' Instability

The second type of instability found in SMF flows to be investigated here was the 'shedding-type' instability which is present in numerous bluff body wakes, as discussed by Sigurdson (1995b). It was found the 'shedding-type' instability has a constant St_{shed}, which is defined as Equation 1.5. Since the field of view was restricted above the fence in the thin BL case shown in Figure 3.1, the maximum height of the recirculation region (Y_b) could be lower than the real value. This lower Y_b can cause an error when scaling the shedding frequency (f_{shed}) in the thin BL case. Therefore, the thick BL case was only analysed for the 'shedding type' instability to get an accurate St_{shed}. Hence, using Equation 1.5 and the Y_b and U_s values of the thick BL case, f_{shed} can be approximated. The frequency in the

thick BL case is calculated as $f_{shed} = 0.2065$ Hz, which is the 'shedding' structure frequency interested in the 'shedding-type' instability analysis. This means only 2.33 cycles of the large scale 'shedding' structures are possibly present during the total measurement time series of 11.28 seconds. Therefore, the total measurement time is not sufficient to resolve the 'shedding-type' instability by a FFT analysis. For this reason, the Empirical Mode Decomposition (EMD) discussed by Boudraa and Cexus (2007) is used to investigate the 'shedding-type' instability mode.

In order to determine the 'shedding-type' instability, time-series of the streamwise fluctuating velocity component, $u'(x, t)$, were extracted and analysed. The fluctuating velocity component was obtained by subtracting the temporal mean of the series, $\overline{u(x)}$, from each time instant. A point close to reattachment $x = 12.9h, y = 0.38h$ for the $\delta/h = 4.38$ case will be used to illustrate the method. The EMD is employed to analyze the oscillations present in $u'(x, t)$. The EMD method is based on the idea that any fluctuating data set can be decomposed by a finite and a small number of component functions, which are called the intrinsic mode functions (IMF). An IMF is a function with the following requirements; shown by Boudraa and Cexus (2007):

1. In the whole data set, the number of extrema equals the number of zero-crossings.

2. At any point of the horizontal axial, the mean value of the envelope defined by the local maxima and the envelope defined by the local minima is zero.

The procedures to determine the IMF's are outlined in the following steps:

1. Find all the local maxima points in the original data set $(u'(x, t))$ and connect all the local maxima points with a cubic spline line to create the upper envelope.

36

2. Repeat procedure 1 to connect the local minima points of the original data set to create the lower envelope.

3. The mean value of the upper and lower envelopes is m_1. The difference between the original data set $u'(x, t)$ and m_1 can be the first component h_1 if h_1 satisfies the definition of an IMF. The first component is defined as $h_1 = u'(x, t) - m_1$.

4. The next steps are repeated as step 1 to 3 by using the residue function as the original data set. The residue function is defined as: $r_1 = u'(x, t) - h_1$, where h_1 stands for the first IMF component.

After all the components satisfy the IMF definitions, the original data set can be written as:

$$u'(x, t) = \sum_{1}^{n} h_j + r_n. \tag{3.5}$$

After calculation according to the procedures above, 10 IMF's are found from the $u'(x, t)$ time series at $x = 12.9h, y = 0.38h$. Figure 3.8 shows the 10 IMF's. It is evident from Figure 3.8 that the frequency of oscillation reduces with increasing mode number. Therefore, with a-priori knowledge of f_{shed} from the analysis of the time-averaged flow fields, an IMF corresponding to the 'shedding-type' instability can be determined. Consulting Figure 3.8 once more, the 9th IMF equates well to the period of the 'shedding-type' instability calculated by the St_{shed}.
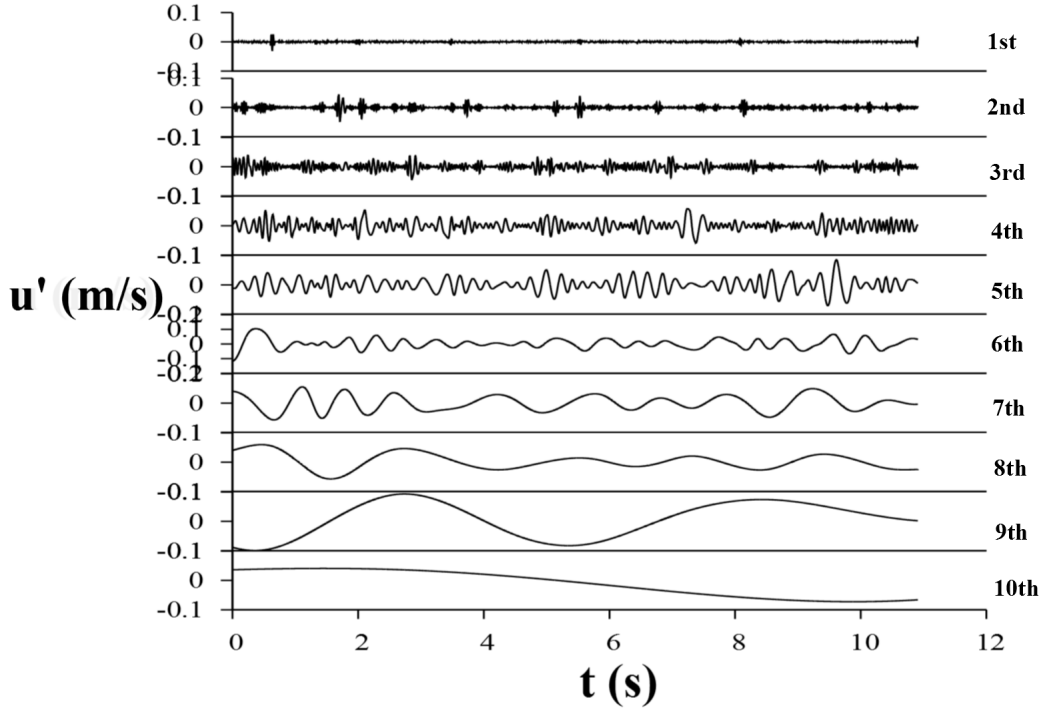
Figure 3.8: Ten IMF's extracted from the fluctuating velocity at the spatial point of $x = 12.9h, y = 0.38h$ as a function of time. The 1st IMF to the 10th IMF are listed from the top to bottom in sequence. The 9th intrinsic mode function shows a oscillating frequency that is close to the frequency calculated by the universal St_{shed}.

Figure 3.9 shows $u'(x, t)$ in red with the 9th IMF represented by the black line. The time interval between the first and the second peaks is 5.66 seconds, giving a $f_{shed} = 0.177$ Hz. Inserting this frequency into Equation 1.5 with the derived $Y_b = 0.048$ m and $U_s = 0.11$ m/s, the $St_{shed} = f_{shed}Y_b/U_s = 0.077$ is calculated. This St_{shed} is quite close to the St_{shed} of 0.08 ± 0.01 determined by Sigurdson (1995a). In a similar fashion to (Siller and Fernholz, 2007), I have qualitatively shown that the 'shedding-type' instability is present in the thick BL case by the finding the 'shedding-type' frequency. An order of magnitude analysis will be presented in the following section to determine whether this phenomena could be responsible for the wind ramp events seen at the UoC meteorological mast.
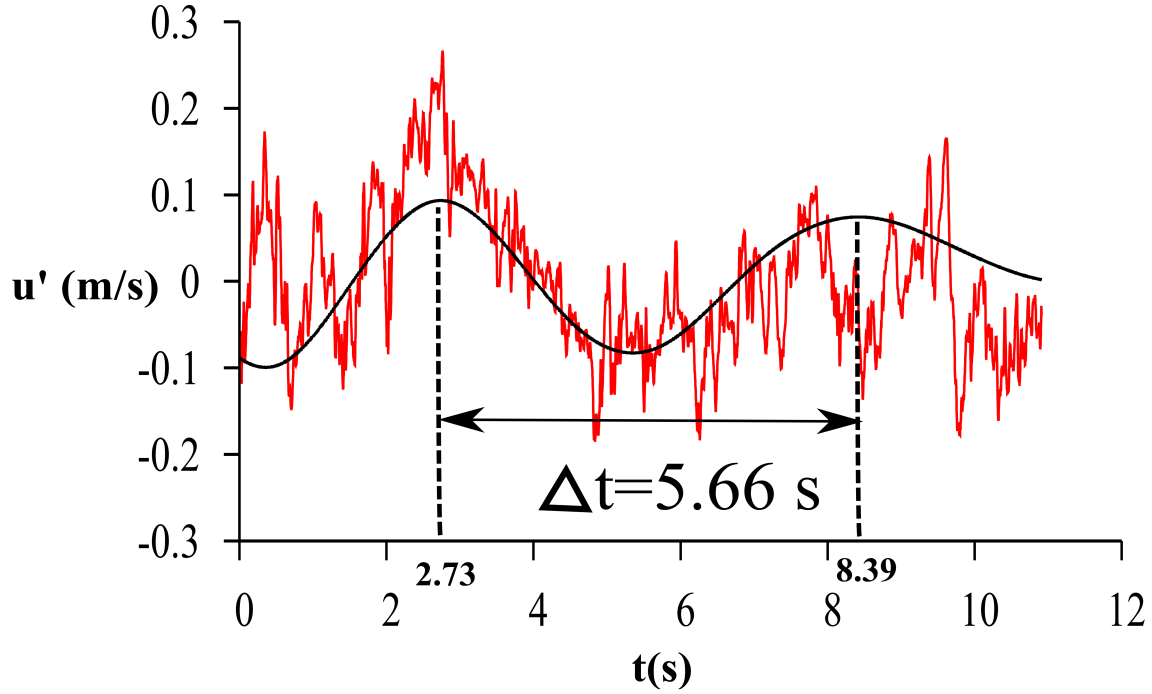
Figure 3.9: The horizontal velocity measured at point $x = 12.9h, y = 0.38h$, as a function of time for the thick BL case. The red line represents the instantaneous velocity fluctuation in the complete measurement time domain. The black line represents the 9th IMF of the data set. The time interval between the two crests is 5.66s, which qualitatively represents the time interval between two consecutive shedding vortex structures.

3.2.3 Order of magnitude analysis of wind ramp events

Based on the 'shedding type' unsteady analysis of the thick BL case, the St_{shed} ($St_{shed} = f_{shed}Y_b/U_s = 0.08$) is applicable to a SMF flow. Since the flow over the mountains contains features which are analogous to a SMF flow, the large scale vortex structures are also expected to exist downstream of the reattachment length in the mountain flow. These shedding structures are a possible cause of the wind ramp events downstream of the Rocky Mountains.

Therefore, the St_{shed} is used to calculate the order of magnitude of the wind ramp time interval. The averaged wind speed used in the order of magnitude analysis of the Rocky Mountain was calculated from the wind rose, as shown in Figure 3.10. The data shown in Figure 3.10 was a hourly-data measured in 2 years by Environment Canada Wind Station, which is located on the top of Nakiska.
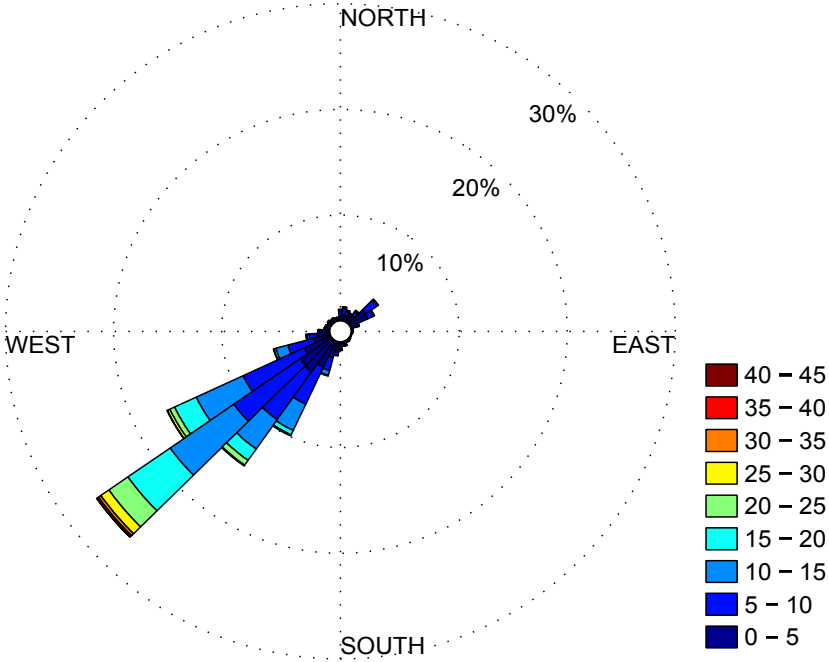
Figure 3.10: Wind rose measured by Environment Canada Wind Station located on the top of Nakiska (Latitude: 50.94, Longitude: -115.19). The wind rose shows the dominant wind direction is 55° from west direction, which is perpendicular to the ridges of the Rocky Mountain. The averaged wind speed is around 10.75 m/s and the standard deviation is around 6.298 m/s.

In Figure 3.10, it shows the dominant wind direction has an angle of 55° from west

direction and is perpendicular to the ridges of the Rocky Mountains. The averaged wind speed calculated from Figure 3.10 is around 10.75 m/s and the standard deviation is around 6.298 m/s. The mountains closest to Calgary are approximately 3000 m above sea level and Calgary is around 1000 m above sea level. Therefore, the height of the mountains closest to Calgary can be approximated as 2000 m ($h \approx 2000$ m). Based on Table 3.1, the maximum height of the recirculation region (Y_b) in the thick BL case is 2.3 h. Hence, the Y_b in the mountain scale can be approximated as 4600 m. When the St_{shed} is used in a mountain scale with height of $h = 4600$ m and a wind speed of $u = 10.75$ m/s, the shedding structure frequency can be calculated as $f_{shed} = 0.000187$ Hz, leading to a time interval of the shedding structure of about 1.49 hours. When the standard deviation of the wind speed is considered, the time interval of the shedding structure fluctuates in between 0.94 hours and 3.59 hours. The wind mast of the Uiversity of Calgary found short ramp events with several time intervals (1~2-hour event, 2~4-hour event and 4~6-hour event). In study of the relaxation region downstream of a SMF by Petryk and Brundrett (1967), it showed that the turbulent boundary layer profile in region from the fence position to $x/h = 100$ is not equilibrium, which illustrated that the convection of the 'shedding' structure from the recirculation region has an effect on the turbulent boundary layer development. This can be used as an evidence of the existence of the shedding vortex structure before $x/h = 100$. Hence, the shedding structure from the recirculation region downstream of the mountains can be expected to exist at Calgary located at $50h$ downstream of the Rocky Mountains. Therefore, based on an order of magnitude analysis, the 'shedding-type' structure downstream of the reattachment point can be related to the possible reason of the wind ramp events downstream of mountains.

Chapter 4

Conclusions

The flow over a SMF with two boundary-layer thickness to fence height ratios was measured using PIV to investigate the steady and unsteady flow features downstream of the fence.

4.1   Time-averaged conditions

The steady features of the flow downstream of the fence were analysed by the time-averaged velocity, vorticity and the turbulent intensity fields, *e.g.* see Figures 3.1, 3.4 and 3.5. It was seen from Figure 3.1 that the thick BL case generated a longer reattachment length than the thin BL case. This was because the higher velocity at the fence separation point in the thick BL case made a higher perturbation. From Figure 3.4, it was shown that the vorticity magnitude in the shear layer of the thin BL case is higher than the thick BL case. This occurred since a higher percentage of vorticity from the incoming boundary layer was available into the shear layer in the thin BL case. Furthermore, the velocity gradient at the fence edge, where the vorticity is generated, was higher in the thin BL case. Turbulent intensity field showed that higher level of Tu was higher in the thin BL case than in the thick BL case, which is due to higher velocity gradient based on Boussinesq approximation.

4.2   Unsteady analysis

After the time-averaged results of the two cases were compared, the vortex dynamics were analysed downstream of the SMF. This included both the K-H instability and the 'shedding type' instability.

The K-H instability was analysed using an FFT analysis of the fluctuating velocity components in the shear layer. It was found that the Strouhal number associated with the K-H

instability, St_h, was higher in the thin BL case compared to the thick BL case. It was also shown that the vortex pairing events in the shear layer occurred further upstream in the thin BL case. This is due to the three-dimensional effects with a reduced width aspect ratio in the thin BL. As the length of the measurement time series was not sufficient for a FFT analysis, the 'shedding type' instability was analysed by the EMD technique. The stream-wise fluctuating velocity component was extracted at a point close to reattachment for the thick BL case. The period of the low frequency fluctuation attributable to the large scale vortex shedding from the recirculation region was 5.66 seconds. The Strouhal number of the 'shedding type' instability, St_{shed}, based on the separation height, velocity at separation and the frequency found, was $St_{shed} = 0.077$. This St_{shed} is close to the $St_{shed} = 0.08 \pm 0.01$ found by Sigurdson (1995a). Based on this St_{shed}, an order of magnitude analysis of the flow over the Rocky Mountains was undertaken. Using a maximum height of the recirculation region downstream of the mountain of 4600 m and a velocity at separation of 10.75 m/s with a standard deviation of 6.298 m/s and scaling to St_{shed} resulted in 'shedding type' instability period of 1.49 hours with a fluctuating period between 0.94 hours and 3.59 hours. Comparing this period and the short wind ramp events measured 50 h downstream of the Rocky Mountains, the large scale structures created by the 'shedding type' instability are a feasible cause of the wind ramp events.

4.3   Recommendation and Future Work

In the current work, a 2D flow over a single fence was measured with different inlet boundary layer thickness. However, the use of multi-fences was not taken into consideration whereupon multi-fences can be employed to represent rows of mountain ridges. The flow downstream of the last fence in the multi-fences scenario can be seen as a manipulated flow condition due to the effect of upstream fences. Therefore, one important parameter in multi-fence flow is the distance between fences. In the simulation study by Orellano and Wengle (2000), flow over a SMF was manipulated by injecting fluid at $3h$ upstream of the fence. Two injection frequencies were applied corresponding to $St_h = 0.6$ and $St_h = 0.08$ respectively. The high forcing frequency case of $St_h = 0.6$ showed the influence of the separated shear layer on vortex roll-up and pairing whereupon the reattachment length was reduced by 10%. In the low-forcing frequency case of $St_h = 0.08$, the shear layer affected the behaviour of the entire recirculation bubble where the reattachment length was reduced by 36%. Therefore, it can be assumed that if the distance between fences is changed, different forcing frequency structures will affect downstream fence flow. Hence, the inclusion of multi-fences in future studies is certainly warranted.

Bibliography

Adams, E. and Johnston, J. (1988). Effects of the separating shear layer on the reattachment flow structure part 2: Reattachment length and wall shear stress. *Experiments in Fluids*, 6(7):493–499.

Armaly, B., Durst, F., Pereira, J., and Schonung, B. (1983). Experimental and theoretical investigation of backward-facing step flow. *J. Fluid Mech*, 127(473):20.

Boudraa, A.-O. and Cexus, J.-C. (2007). Emd-based signal filtering. *Instrumentation and Measurement, IEEE Transactions on*, 56(6):2196–2202.

Bradshaw, P. (1966). The effect of initial conditions on the development of a free shear layer. *J. Fluid Mech*, 26(2):225–236.

Browand, F. K. (1966). An experimental investigation of the instability of an incompressible, separated shear layer. *Journal of Fluid Mechanics*, 26(02):281–307.

Castro, I. and Fackrell, J. (1978). A note on two-dimensional fence flows, with emphasis on wall constraint. *Journal of Wind Engineering and Industrial Aerodynamics*, 3(1):1–20.

Chapman, D. R., Kuehn, D. M., and Larson, H. K. (1958). *Investigation of separated flows in supersonic and subsonic streams with emphasis on the effect of transition*, volume 1356. NACA.

Choi, Y. and Kim, H. (2010). Pulsating jet control for manipulating the separation bubble behind the fence. *Journal of Visualisation*, 13:221–228.

Conference, I. T. T. (2008). Uncertainty analysis particle imaging velocimetry.

De Brederode, V. and Bradshaw, P. (1972). *Three-dimensional Flow in Nominally Two-dimensional Separation Bubbles: Flow Behind a Rearward-facing Step. I.* Department of Aeronautics, Imperial College of Science and Technology.

Durst, F. and Tropea, C. (1981). Turbulent, backward-facing step flows in two-dimensional ducts and channels. In *Proc. 3rd Int. Symp. on Turbulent Shear Flows*, pages 18–1.

Eaton, J. and Johnston, J. (1981). A review of research on subsonic turbulent flow reattachment. *AIAA journal*, 19(9):1093–1100.

Freymuth, P. (1966). On transition in a separated laminar boundary layer. *Journal of Fluid Mechanics*, 25:683–704.

Friedrich, R. and Arnal, M. (1990). Analysing turbulent backward-facing step flow with the lowpass-filtered navier-stokes equations. *Journal of Wind Engineering and Industrial Aerodynamics*, 35:101–128.

Good, M. and Joubert, P. (1968). The form drag of two-dimensional bluff-plates immersed in turbulent boundary layers. *Journal of Fluid Mechanics*, 31:547–582.

Huppertz, A. and Fernholz, H.-H. (2002). Active control of the turbulent flow over a swept fence. *European Journal of Mechanics B–Fluids*, 21:429–446.

Kiya, M. and Sasaki, K. (1983). Structure of a turbulent separation bubble. *Journal of Fluid Mechanics*, 137(83):113.

Le, H., Moin, P., and Kim, J. (1997). Direct numerical simulation of turbulent flow over a backward-facing step. *Journal of Fluid Mechanics*, 330(1):349–374.

Leclercq, D. J., Jacob, M. C., Louisot, A., and Talotte, C. (2001). Forward-backward facing step pair: aerodynamic flow, wall pressure and acoustic characterisation. *AIAA paper*, 2249.

Moss, W., Baker, S., and Bradbury, L. (1979). Measurements of mean velocity and reynolds stresses in some regions of recirculating flow. In *Turbulent Shear Flows I*, pages 198–207. Springer.

Neto, A. S., Grand, D., Métais, O., and Lesieur, M. (1993). A numerical investigation of the coherent vortices in turbulence behind a backward-facing step. *Journal of Fluid Mechanics*, 256:1–25.

Orellano, A. and Wengle, H. (2000). Numerical simulations (dns and les) of manipulated turbulent boundary layer flow over a surface–mounted fence. *European Journal of Mechanics B–Fluids*, 19:765–788.

Orellano, A. and Wengle, H. (2001). Pod analysis of coherent structures in forced turbulent flow over a fence. *Journal of Turbulence*, 2. DOI: 10.1088/1468-5248/2/1/008.

Petryk, S. and Brundrett, E. (1967). Recovery of a turbulent boundary layer by a single roughness element. Technical report, Final Report No.

Raffel, M., Willert, C. E., and Kompenhans, J. (1998). *Particle Image Velocimetry: A Practical Guide; with 24 Tables.* Springer.

Sevlian, R. and Rajagopal, R. (2012). Wind power ramps: Detection and statistics. In *Power and Energy Society General Meeting, 2012 IEEE*, pages 1–8. IEEE.

Sherry, M., Lo Jacono, D., and Sheridan, J. (2010). An experimental investigation of the recirculation zone formed downstream of a forward facing step. *Journal of Wind Engineering and Industrial Aerodynamics*, 98(12):888–894.

Sigurdson, L. (1995a). The structure and control of a turbulent reattaching flow. *Journal of Fluid Mechanics*, 298(1):139–165.

Sigurdson, L. (1995b). The structure and control of a turbulent reattaching layer. *Journal of Fluid Mechanics*, 298:139–165.

Siller, H. and Fernholz, H. (1996). Control of the separated flow downstream of a two-dimensional fence by low-frequency forcing. *Applied scientific research*, 57(3-4):309–318.

Siller, H. and Fernholz, H.-H. (1997). Control of the separated flow downstream of a two-dimensional fence by low-frequency forcing. *Applied scientific research*, 57:309–318.

Siller, H. and Fernholz, H.-H. (2007). Manipulation of the reverse-flow region downstream of a fence by spanwise vortices. *European Journal of Mechanics B–Fluids*, 26:236–257.

Timmins, B. H., Wilson, B. W., Smith, B. L., and Vlachos, P. P. (2012). A method for automatic estimation of instantaneous local uncertainty in particle image velocimetry measurements. *Experiments in fluids*, 53(4):1133–1147.

Wilson, B. M. and Smith, B. L. (2013). Uncertainty on piv mean and fluctuating velocity due to bias and random errors. *Measurement Science and Technology*, 24(3):035302.

Winant, C. and Browand, F. (1974). Vortex pairing- the mechanism of turbulent mixing-layer growth at moderate reynolds number. *Journal of Fluid Mechanics*, 63(2):237–255.

Yang, Z. and Voke, P. R. (2001). Large-eddy simulation of boundary-layer separation and transition at a change of surface curvature. *Journal of Fluid Mechanics*, 439:305–333.

Appendix A

Uncertainty Analysis of PIV

The particle image velocimetry (PIV) measurement technique is a robust method to record the flow field in fluid mechanics experiments. It presents with a number of advantages which will be outlined in the following section:

Firstly, compared to more established experimental techniques such as hot wire anemometers or pressure tubes that apply probes to measure the velocity field, PIV is a non-intrusive optical measurement technique. This is a clear advantage over the aforementioned intrusive techniques. Secondly, PIV typically measures a large proportion of the flow field at once, *i.e.* the velocity field can be resolved spatially and temporally.

As summarized by Raffel et al. (1998) and shown in Figure A.1, a PIV system consists of several components.

Figure A.1: Basic setup of a PIV system, as shown by Raffel et al. (1998).

Neutrally buoyant tracer particles which follow the fluid well are first added to the flow. A laser sheet illuminates the plane of interest. The laser sheet can either be generated using a pulsed system where particles are illuminated by two pulses over a short time interval or using a continuous output system. The light scattered by the tracer particles denotes their instantaneous positions. The scattered light is recorded by a digital camera either on a single

frame (double exposure) or on a sequence frames (single exposure). A continuous laser and single exposure images were used in the current investigation. The tracer particles travel a displacement over the time interval between the two images, which is a controlling PIV parameter.

The processing of the digital PIV recording is completed in small sub-areas of the image field, known as interrogation windows. The local displacement vector is then determined in each interrogation window by a cross-correlation algorithm. The velocity vector of each interrogation window can then be determined with knowledge of the time interval between images.

A.1   The PIV measurement error analysis

However, as a measurement system, PIV has sources of error. The error of the current PIV measurements will be discussed in the following section. There are many sources of error that can affect the accuracy and the uncertainty of PIV, such as the system calibration, timing errors, system setup, particle size to name but a few (Wilson and Smith, 2013).

When a turbulent flow field is measured by PIV, the measured velocity u can be decomposed into the components as shown in Equation A.1:

$$u = \overline{u} + u' + \breve{u} + \beta_u \tag{A.1}$$

where $\overline{u}$ is the mean velocity, u' is the fluctuation velocity, $\breve{u}$ is the random error and β_u is the systematic error as indicated by Wilson and Smith (2013).

The measurement uncertainty represents the range within which we can expect to find the true error based on probability. The random error component results in precision uncertainty on time-averaged quantities derived from a finite number of samples Wilson and Smith (2013). Therefore, in PIV measurements, the precision uncertainty refers to the mean quantities.

Although the uncertainty of the mean values that is caused by velocity fluctuation and noise from PIV can be reduced by measuring for a longer time period, in doing so, the random measurement error can cause a bias to the Reynolds stress or the fluctuating velocity quantities. In the PIV technique, the error is affected by the particle density, particle diameter, pixel displacement and velocity gradients in the flow field.

The error caused by pixel displacements less than the particle image diameter is controlled by the PIV systems settings. Image diffraction through the lens aperture also strongly affects the particle diameter (Wilson and Smith, 2013). When the particle image diameter changes, the change in the time-averaged velocity is negligible but the fluctuating velocity quantities change.

Particle image density is defined as the average number of particles per interrogation window (Wilson and Smith, 2013). In most cases, the effects of particle density on the time-averaged velocity and the fluctuating velocity can be neglected. However, when measuring shear regions and the particle density is low, the signal to noise ratio will reduce due to the insufficient seeding (Timmins et al., 2012). Timmins et al. (2012) found that instantaneous velocity gradients can result in the largest uncertainties.

Table A.1: Parameter settings of PIV processing with DaVis 8 software

Parameters	Units	Thin BL	Thick BL
Image frame rates	frame/sec	125	500
Time interval between images	second	0.008	0.002
Laser sheet thickness	mm	2	2
Magnification factor (MF)	pixel/mm	4.84	14.62
Initial interrogation window	pixel	128×128	128×128
Final interrogation window	pixel	16×16	16×16
Interrogation window overlap	%	75	75
Optimal particle displacement	pixel	8	8
Max u velocity	m/s	0.15	0.33
Max particle displacement	pixel	5.81	8.57

From Table A.1, in the thin boundary-layer case, the maximum particle displacement calculated as a function of the 1/4 rule was 5.81 pixels. The in-plane particle losses between images is therefore minimized. However, in the thick boundary-layer case, the particle displacement between images based on my imaging parameters was 8.67 pixels, which was slightly larger than the suggested 1/4 displacement rule. To reduce displacement lower than 8 pixels, higher frames rates or a larger interrogation window size could have been employed.

In the measurements presented here, only the dominant sources of systematic error are taken into consideration. For my measurements, calibration of the cameras was completed using a calibration board aligned to the laser sheet plane. Therefore, the angle between the calibration board and the laser sheet plane (θ) will lead to a systematic error. Since turbulent flow is three dimensional, the out-of-plane velocity is not measured directly by 2D PIV measurements. Therefore, the out-of-plane velocity component is an unavoidable source of error when a turbulent flow is measured in a two-dimensional plane. For a derived

parameter, its value can be defined as:

$$R = f(x_1, x_2, x_3, ..., x_n), \tag{A.2}$$

where R is the derived parameter and x_n are the related parameters. The uncertainties ω_R of the derived parameter R can be written as:

$$\omega_R = \sqrt{\sum_{i=1}^{n}(\omega_{x_i}\frac{\partial R}{\partial x_i})^2}, \tag{A.3}$$

$$\omega_x = \sqrt{P_x^2 + B_x^2}, \tag{A.4}$$

where ω_{x_i} is the uncertainty of each related parameter, ω_R is the uncertainty of the derived parameter R, P_x is the random component of uncertainty and B_x is the systematic component of uncertainty.

In the flow field shown in Figure 3.1, the uncertainty of the measured velocity u is determined as:

$$u = MF(\Delta X/\Delta t) + \delta_u, \tag{A.5}$$

where u is the measured velocity, MF is the magnification factor, ΔX is the particle displacement between images in pixels, Δt is the time interval between each image in seconds and δ_u is the out-of-plane velocity component in the measurement plane. The uncertainty of parameters MF and δ_u will be analysed in the following sections.

As discussed in Conference (2008), the calibration MF can be expressed as:

$$MF = l_r \cos \theta / L_r \approx l_r(1 - \theta^2)/L_r, \tag{A.6}$$

where l_r is the length of physical domain (mm), θ is the angle between the laser plane and the calibration board (and L_r is the length in the image plane (pixels). Therefore, in the measurements presented here, as $l_r = 120mm$ and $L_r = 599pixel$, MF will equal 4.99 pixel/mm.

As mentioned by Conference (2008), the uncertainty of the physical length is less than $20\mu m$ or 0.02 mm. The sensitivity factor can be calculated as:

$$\frac{\partial MF}{\partial l_r} = 1/L_r = 1/599 = 1.669 \times 10^{-3}(1/pixel), \tag{A.7}$$

Based on the discussion by Conference (2008), the total uncertainty will be 0.7 pixels when measuring the length of the image starting from single reference points. The sensitivity factor can be calculated as:

$$\frac{\partial MF}{\partial L_r} = -l_r/L_r^2 = -120/599^2 = -3.34 \times 10^{-4}(mm/pixel^2), \tag{A.8}$$

Lens aberration will also cause image distortion which can be quantified (Conference, 2008). The distortion of the image will be less than 0.5%, and 29.95 pixels. The sensitivity factor is calculated as:

$$\frac{\partial MF}{\partial L_r} = -l_r/L_r^2 = -120/599^2 = -3.34 \times 10^{-4}(mm/pixel^2), \tag{A.9}$$

Ideally, the calibration board should be coplanar with the laser sheet plane. Assuming a maximum angle $\theta = 20.035rad$, the sensitivity factor is:

$$\frac{\partial MF}{\partial \theta} = -l_r \times \theta/L_r = -120 \times 0.035/599 = -7.0117 \times 10^{-3}(mm/pixel), \tag{A.10}$$

As the planar measurement technique was applied in a turbulent flow, the 3-dimensional effects on the 2-dimensional velocity field must be taken into account. With the out-of-plane velocity component, the measured in-plane velocity can be written as:

$$u_m = u + wtan\alpha, \tag{A.11}$$

where u_m is the total measured velocity, u is the in-plane velocity, w is the out-of-plane velocity and $w\tan\alpha$ is the out-of-plane velocity component in the measurement plane. Conference (2008) suggests the out-of-plane velocity can be assumed as 1.0% of the freestream velocity. Based on this, it is assumed that $w = 100 \times 0.01 = 1(mm/s)$. The uncertainty can be calculated as $100 \times 0.01 \times \tan(205.2/850) = 4.21 \times 10^{-6}(mm/s)$.

With the uncertainty of related parameters calculated above, the uncertainty of the MF and the out-of-plane velocity can be calculated using the method of uncertainty propagation. The uncertainty of MF and the out-of-plane velocity can be calculated as:

$$\omega_{MF} = \sqrt{\sum_{i=1}^{n}(\omega_{x_i}\frac{\partial MF}{\partial x_i})^2} = 0.049987(mm/pixel) = 24.94(mm/s). \tag{A.12}$$

Therefore, the combined uncertainty with consideration of MF and the out-of-plane velocity can be calculated as:

$$\omega = \sqrt{\omega_{MF}^2 + \omega_{\delta_u}^2} = \sqrt{24.94^2 + (4.21 \times 10^{-6})^2}(mm/pixel) = 24.94(mm/s), \tag{A.13}$$

when a coverage factor of two is considered in the combined uncertainty, a 95% confidence interval gives an expanded uncertainty of 49.89 mm/s.